

RESEARCH ARTICLE

10.1002/2016JC012400

Key Points:

- Oscillatory winds induce episodic deep mixing, nutrient entrainment, and phytoplankton growth at fronts in nutrient-limited oceans
- Low-frequency and high-frequency winds have a synergistic and greater impact on nutrient entrainment and phytoplankton on the less dense side of fronts
- The synergistic phytoplankton response to low-frequency and high-frequency winds relies on the high-frequency wind just below the Coriolis frequency

Supporting Information:

- Supporting Information S1

Correspondence to:

D. B. Whitt,
dan.whitt@gmail.com

Citation:

Whitt, D. B., M. Lévy, and J. R. Taylor (2017), Low-frequency and high-frequency oscillatory winds synergistically enhance nutrient entrainment and phytoplankton at fronts, *J. Geophys. Res. Oceans*, 122, 1016–1041, doi:10.1002/2016JC012400.

Received 29 SEP 2016

Accepted 15 DEC 2016

Accepted article online 26 DEC 2016

Published online 10 FEB 2017

Low-frequency and high-frequency oscillatory winds synergistically enhance nutrient entrainment and phytoplankton at fronts

D. B. Whitt ¹, M. Lévy ², and J. R. Taylor ¹

¹Department of Applied Mathematics and Theoretical Physics, University of Cambridge, Cambridge, UK, ²Sorbonne Université (UPMC Paris 6/CNRS/IRD/MNHN), LOCEAN-IPSL, Paris, France

Abstract When phytoplankton growth is limited by low nutrient concentrations, full-depth-integrated phytoplankton biomass increases in response to intermittent mixing events that bring nutrient-rich waters into the sunlit surface layer. Here it is shown how oscillatory winds can induce intermittent nutrient entrainment events and thereby sustain more phytoplankton at fronts in nutrient-limited oceans. Low-frequency (i.e., synoptic to planetary scale) along-front wind drives oscillatory cross-front Ekman transport, which induces intermittent deeper mixing layers on the less dense side of fronts. High-frequency wind with variance near the Coriolis frequency resonantly excites inertial oscillations, which also induce deeper mixing layers on the less dense side of fronts. Moreover, we show that low-frequency and high-frequency winds have a synergistic effect and larger impact on the deepest mixing layers, nutrient entrainment, and phytoplankton growth on the less dense side of fronts than either high-frequency winds or low-frequency winds acting alone. These theoretical results are supported by two-dimensional numerical simulations of fronts in an idealized nutrient-limited open-ocean region forced by low-frequency and high-frequency along-front winds. In these model experiments, higher-amplitude low-frequency wind strongly modulates and enhances the impact of the lower-amplitude high-frequency wind on phytoplankton at a front. Moreover, sensitivity studies emphasize that the synergistic phytoplankton response to low-frequency and high-frequency wind relies on the high-frequency wind just below the Coriolis frequency.

1. Introduction

The oceanic reservoir of carbon and the flux of carbon between the atmosphere and ocean depend on primary production by ocean phytoplankton in the euphotic zone, which is intimately linked to the upward physical transport of nutrients to the euphotic zone from large reservoirs in the ocean interior [e.g., Volk and Hoffert, 1985; Raven and Falkowski, 1999; Gruber and Sarmiento, 2002]. Process studies suggest that mesoscale (100–10 km) and submesoscale (10–1 km) dynamics may play an important role in modulating the vertical flux of nutrients to the euphotic zone [see reviews by Martin, 2003; Klein and Lapeyre, 2009; Lévy et al., 2012a; McGillicuddy, 2016; Mahadevan, 2016], and therefore the global biological pump. However, the net effect of mesoscale or submesoscale processes on regional and global scale nutrient fluxes to the euphotic zone in oligotrophic oceans [e.g., Oschlies, 2002; Lévy et al., 2012b], or elsewhere [e.g., Strass et al., 2002; Gruber et al., 2011], remains a subject of active debate.

Mesoscale and submesoscale oceanic variability is characterized by a wide variety of phenomena at the ocean surface, including fronts, jets, filaments, and eddies among others [see the aforementioned reviews]. However, this paper focuses exclusively on fronts [e.g., Fedorov, 1986], which are ubiquitous [e.g., Belkin et al., 2009] and associated with anomalous biogeochemistry. For example, high-resolution observations of the biogeochemical constituents across fronts reveal elevated nutrients, stronger upward nutrient fluxes, stronger downward organic carbon export, higher chlorophyll, more full-depth-integrated biomass, and different plankton community composition at fronts [e.g., Claustre et al., 1994; Granata et al., 1995; Fernández and Pingree, 1996; Allen et al., 2005; Niewiadomska et al., 2008; Davis et al., 2008; Li et al., 2012; Taylor et al., 2012; Guidi et al., 2012; Powell and Ohman, 2015; Krause et al., 2015]. Hence, it is possible that frontal dynamics plays a significant role in setting the integrated rates and reservoirs of global biogeochemical cycles by modifying the oceanic biological pump. Thus, understanding and quantifying the local and remote effects

of frontal dynamics on ocean biogeochemistry in general, and upward nutrient fluxes and phytoplankton dynamics in particular, is an important fundamental and practical scientific objective.

Here we specifically consider how vertical nutrient fluxes and phytoplankton dynamics are modified by unsteady winds over geostrophic density fronts in midlatitude open oceans, where phytoplankton growth at the surface is limited by nutrients that are replete at depth (henceforth, this specific context is assumed unless otherwise specified). Several published studies have identified the wind as a prominent driver of variability in phytoplankton and nutrients at fronts. In particular, winds drive deeper surface mixing layers (SXLs) [e.g., *Franks and Walstad*, 1997; *Lévy et al.*, 2009] and stronger vertical motions [e.g., *Franks and Walstad*, 1997; *Mahadevan et al.*, 2008; *Nagai et al.*, 2008; *Lévy et al.*, 2009] at fronts, both of which enhance upward nutrient fluxes and phytoplankton growth at fronts. However, although some prior numerical process studies have presented simulations of biogeochemistry in fronts forced by unsteady winds [e.g., *Franks and Walstad*, 1997; *Lévy et al.*, 2009], it is not well understood how nutrient fluxes or phytoplankton at a front depend on the details of the unsteadiness (i.e., the frequency content and direction of the oscillatory part of the wind).

No published study that we know of has explicitly investigated how nutrients and phytoplankton respond to an oscillatory wind (i.e., an unsteady wind with zero time mean) at a front in the open ocean. This manuscript addresses this gap by presenting some results from a numerical process study of physics and biogeochemistry under oscillatory winds at a front in an idealized nutrient-limited open-ocean domain in the midlatitudes. We further narrow the scope of this paper by focusing on how the physics of the wind-driven SXL drives spatially and temporally heterogeneous nutrient entrainment across the front, and thereby affects the distribution of phytoplankton at the front.

Section 1.1 presents the prior results and theory that lead to the specific questions and approach of this paper. Section 1.2, largely independent of section 1.1, presents the questions to be addressed, the computational approach that will be taken in answering them, and the outline of the remainder of the paper.

1.1. Background, Hypotheses, and Theory

Section 1.1.1 summarizes the results of previous modeling studies that explicitly discuss the effect of unsteady winds on SXLs, nutrients, and phytoplankton at open-ocean fronts; these results lead to the central hypothesis of this paper. Sections 1.1.2 and 1.1.3 present theoretical ideas that support the hypothesis of this paper, demonstrate the need for numerical experiments, and motivate the metrics to be used while analyzing the results.

1.1.1. Background

In a seminal study, *Franks and Walstad* [1997] explore the formation of subsurface phytoplankton patches at a front using idealized two-dimensional numerical simulations. In particular, they show that 1 day wind bursts oriented parallel to the front (i.e., along-front) drive a cross-front Ekman transport that modifies SXL depths in the front. Compared to all other wind directions, down-front winds (i.e., winds pointed in the direction of the geostrophic frontal jet), which drive an Ekman transport of denser water over lighter water at the front, induce the deepest SXLs, most entrainment, and highest phytoplankton concentrations in the SXL at the front.

Three-dimensional simulations of physics and biogeochemistry at idealized meandering fronts by *Lévy et al.* [2009] show that even when fronts are highly deformed by three-dimensional baroclinic instability, several days of steady wind drives a transient increase in phytoplankton concentrations and primary productivity at fronts. When oscillations near the Coriolis frequency at an amplitude equal to the mean wind are added, the domain-integrated increase in new primary production is significantly greater than under steady wind alone. Moreover, there is a pronounced increase in new production in the SXL, which is significantly deeper under high-frequency wind and deepest in the vicinity of the submesoscale fronts.

In an unpublished manuscript, henceforth WTL, we explore how vertical advection modifies biogeochemistry at a front under oscillatory wind with periods characteristic of low-frequency synoptic to planetary-scale atmospheric variability (i.e., 4–16 day oscillations) over several forcing periods (i.e., a couple months) of simulated time and amplitudes ranging from 0.06 to 0.24 N/m². Although WTL focus on scenarios where the deepest SXLs do not reach the nutricline and hence vertical advection in the pycnocline sustains the biogeochemical response, the results show that SXLs are intermittently deepest on the less dense side of the front.

Here we explicitly consider the biogeochemical impacts of combining higher-amplitude low-frequency wind with lower-amplitude high-frequency wind, both of which are present in all real wind stress time series and together may result in significantly deeper SXLs and more nutrient entrainment into the SXL at the front than low-frequency wind acting alone.

The motivating hypotheses, explained in more detail in sections 1.1.2 and 1.1.3, respectively, are:

1. Phytoplankton in nutrient-limited oceans respond nonlinearly to increases in SXL depths as the SXL penetrates the nutricline and turbulent mixing increases the nutrient concentration in the SXL [e.g., *Marra et al.*, 1990]. Hence, intermittent deep surface mixing is responsible for sustaining a significant fraction of the full-depth-integrated phytoplankton biomass and primary production in nutrient-limited oceans [e.g., *Lévy et al.*, 2009; *Carranza and Gille*, 2015; *Nicholson et al.*, 2016].
2. SXLs are spatially and temporally heterogeneous [e.g., *Lévy et al.*, 2009; *Kouketsu et al.*, 2012; *Carranza and Gille*, 2015; *Thompson et al.*, 2016]. Anomalously deep SXLs can be formed by—among other processes—an interaction between fronts and oscillatory winds.

Together these two notions lead to the central hypothesis of this paper: low-frequency and high-frequency oscillatory winds synergistically enhance nutrient entrainment and phytoplankton at fronts.

1.1.2. How Phytoplankton Respond to Intermittent Surface Mixing

Insights into the biogeochemical response to intermittent surface mixing are derived from a well-tested and well-constrained, albeit simplified, four-component NPZD (nutrient, phytoplankton, zooplankton, and detritus, respectively) ecosystem modeling framework [e.g., *Doney et al.*, 1996; *Spitz et al.*, 2003; *Powell et al.*, 2006]. Note that all four constituents are referred to in the same nutrient-based units, that is mmol N/m^3 . The governing equations of the ecosystem model and parameter values are provided in supporting information.

In an NPZD model, phytoplankton exist in a delicate balance between growth via primary production, which is facilitated by upward nutrient fluxes, and loss via senescence and zooplankton grazing. Losses are then remineralized into nutrient again at deeper depths due to detrital sinking. In a steady state with modest vertical diffusivities $K_z \sim 10^{-5} \text{ m}^2/\text{s}$ characteristic of the ocean pycnocline and no advecting velocities, a biogeochemical equilibrium emerges where vertical sinking of detritus is balanced by the upward diffusive flux of all constituents (which is generally dominated by the diffusive nutrient flux). In this equilibrium, phytoplankton are concentrated at a subsurface phytoplankton maximum (SPM) at about the same depth as the nutricline (e.g., Figure 1). The depth of the SPM is determined primarily by the vertical penetration of the light. See *Cullen* [2015] for a review of SPM phenomenology, *Beckmann and Hense* [2007] for parametric studies of SPM equilibrium dynamics, and *Doney et al.* [1996] for an example application.

In one-dimensional simulations with an NPZD model (see supporting information for the equations and parameters used here), intermittent periods of enhanced vertical mixing in an SXL (where the vertical diffusivity $K_z \sim 10^{-2} \text{ m}^2/\text{s}$ is about 3 orders of magnitude higher than the pycnocline diffusivity $K_z \sim 10^{-5} \text{ m}^2/\text{s}$), can disturb the biogeochemical equilibrium at the SPM. However, the impact of an SXL on biogeochemistry depends strongly on the depth of the SXL relative to the nutricline and SPM, as shown in Figures 1 and 2. When the SXL is well above the nutricline, the surface mixing has almost no effect on the biogeochemistry. As the SXL reaches the nutricline and nutrient is entrained into the SXL, the full-depth-integrated phytoplankton growth rate increases rapidly as nutrients are supplied to the nutrient-limited SXL, and there is a significant increase in full-depth-integrated phytoplankton, most of which occurs at relatively low concentrations in the SXL (Figure 1). Zooplankton growth rates are not as rapid as phytoplankton growth rates, hence full-depth-integrated zooplankton increase more slowly than phytoplankton in response to the increase in available resources (Figure 2). Yet, on a time scale of several weeks to a few months, a new cyclostationary equilibrium is achieved with more phytoplankton, more zooplankton, higher nutrient uptake rates, and higher grazing rates (not shown, but see Figure 2).

Hence, we hypothesize that in nutrient-limited open-ocean conditions, regions where anomalously deep SXLs intermittently reach the nutricline are associated with more full-depth-integrated phytoplankton, primarily because of an increase in primary production due to increased nutrient in the euphotic zone. Primary production and zooplankton grazing rates will be diagnosed from numerical simulations to clarify how primary production and zooplankton grazing interact to modify phytoplankton accumulation rates and full-depth-integrated biomass at a front forced by oscillatory winds.

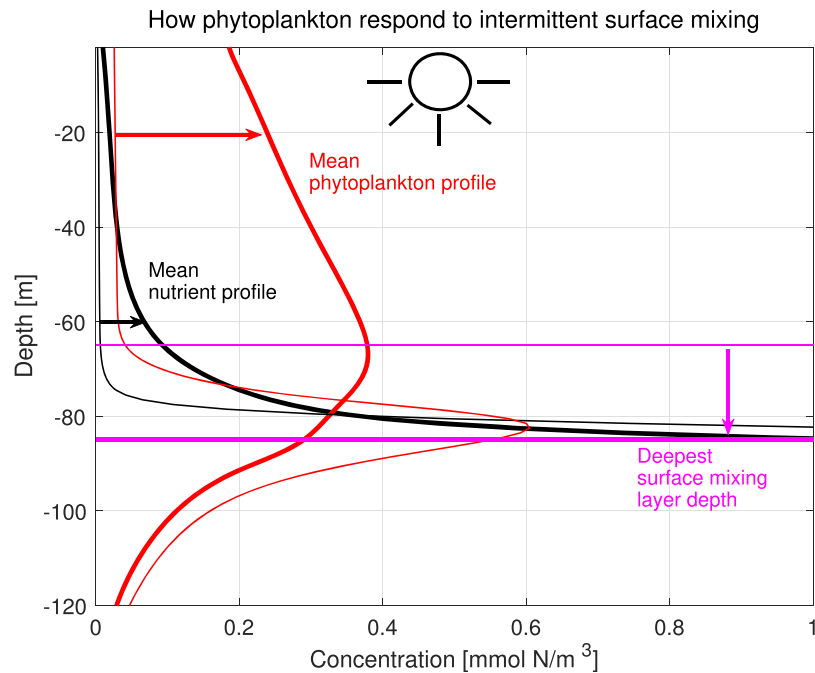


Figure 1. Time-mean phytoplankton (red) and nutrient (black) profiles depend on the depth of the surface mixing layer (magenta) in nutrient-limited oceans. When the deepest surface mixing layer does not reach the equilibrium nutricline depth without surface mixing (i.e., about 80 m here), the nutricline is relatively shallow and sharp, and there is a subsurface phytoplankton maximum at the nutricline (thin lines). When the mixing layer just reaches the equilibrium nutricline, the full-depth-integrated phytoplankton biomass increases dramatically, phytoplankton are distributed across the surface mixing layer, and the maximum phytoplankton concentration is reduced (thick lines). In these results, obtained from one-dimensional simulations of the NPZD model with a variable vertical diffusivity K_z and no advecting velocities, surface mixing is associated with an elevated vertical diffusivity $K_z \sim 10^{-2} \text{ m}^2/\text{s}$ from the surface down to either 65 or 85 m (magenta lines) for 1 day out of every 8 days (see Figure 2). Below the base of the surface mixing layer (and at all depths on the other 7 days), the vertical diffusivity is low $K_z \sim 10^{-5} \text{ m}^2/\text{s}$.

1.1.3. How Oscillatory Winds Induce Anomalous Surface Mixing at Fronts

A proposed source of intermittently deep SXLs in nutrient-limited oceans involves a synergistic physical response to low-frequency and high-frequency oscillatory wind forcing at fronts. We discuss the response to either low or high frequencies acting alone first and then describe their synergistic effects, while referring to the schematic shown in Figure 3.

Low-frequency synoptic-to-planetary scale along-front wind drives cross-front Ekman transport (to the right of the wind in the northern hemisphere, as shown in Figure 3), which modifies the buoyancy and stratification in the front via the horizontal advection of buoyancy by the Ekman flow. This horizontal advection of buoyancy can be quantified via the Ekman buoyancy flux

$$EBF = -\frac{\tau}{\rho_0 f} \times \nabla_h b, \quad (1)$$

[e.g., Franks and Walstad, 1997; Rintoul and England, 2002; Thomas, 2005; Thomas and Ferrari, 2008; Mahadevan et al., 2010; Taylor and Ferrari, 2010] (see Figure 3). In a front, the EBF (1) is simply the cross-front component of the Ekman transport times the horizontal buoyancy gradient at the ocean surface, where τ is the wind stress vector, ∇_h is the horizontal gradient operator, $b = -g\rho/\rho_0$ is the buoyancy, g is the acceleration due to gravity, ρ represents the slight perturbations from the background density of water $\rho_0 = 1000 \text{ kg/m}^3$, $\partial b/\partial z$ is the stratification, and f is the Coriolis frequency. The change in the SXL depth H_s from time t_1 to t_2 due to a constant positive (destratifying) EBF is approximately proportional to the square root of the time-integrated Ekman buoyancy flux, more precisely

$$|H_s(t_2)| \sim \left(|H_s(t_1)|^2 + \int_{t_1}^{t_2} \frac{EBF(s)}{q(s)/f} ds \right)^{1/2}, \quad (2)$$

where $q = \omega_a \cdot \nabla b$ is Ertel's potential vorticity at the SXL base and ω_a is the absolute vorticity vector [e.g., Taylor and Ferrari, 2010]. Periods of down-front wind, reduce the surface buoyancy in the front, deepen the

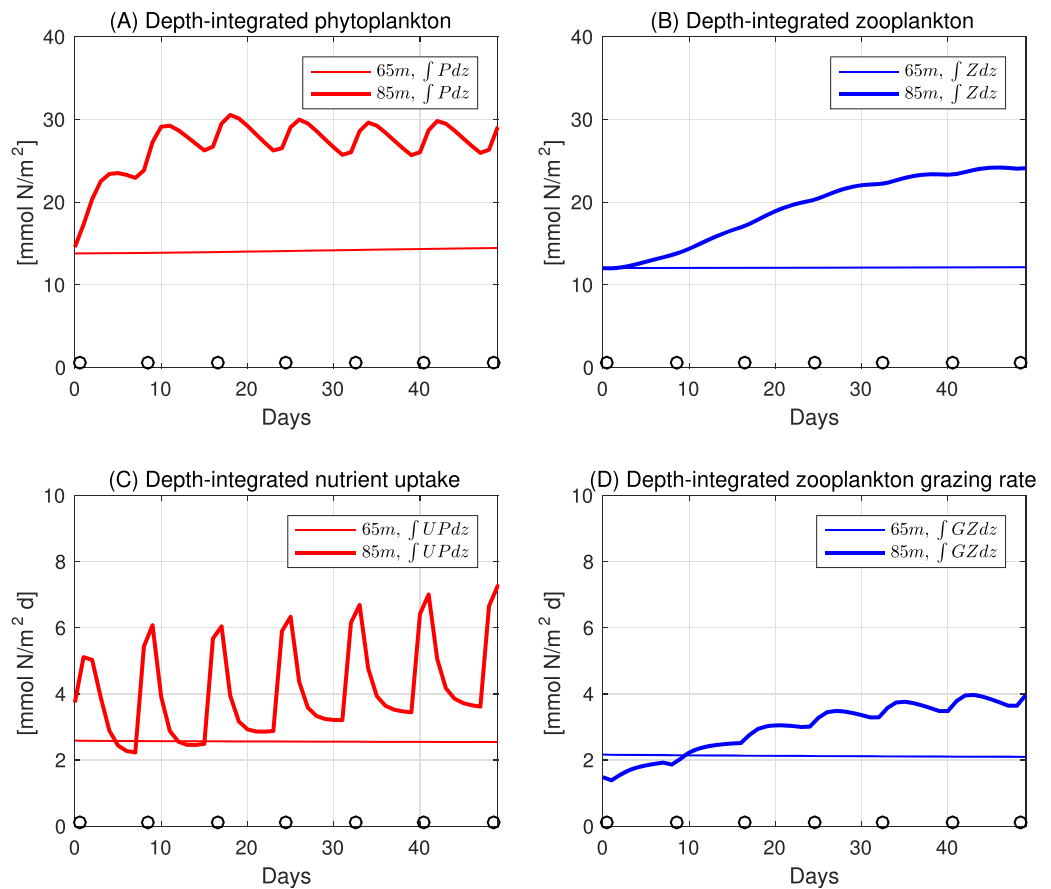


Figure 2. Time series of full-depth-integrated (a) phytoplankton $P_{int} = \int_{z=-H}^0 P dz$, (b) zooplankton $Z_{int} = \int_{z=-H}^0 Z dz$, (c) nutrient uptake rate $UP_{int} = \int_{z=-H}^0 UP dz$, and (d) zooplankton grazing rate $GZ_{int} = \int_{z=-H}^0 GZ dz$, where $H = 1000$ m is the domain depth. Where indicated by the black circles along the x axis, the biogeochemical vertical profile is perturbed by a 1 day long period of enhanced mixing $K_z \sim 10^{-2} \text{ m}^2/\text{s}$ from the surface down to the surface mixing layer depth indicated in the legend. Elsewhere $K_z \sim 10^{-5} \text{ m}^2/\text{s}$. The associated forcing-period-averaged nutrient N and phytoplankton P vertical profiles in the ultimate cyclostationary equilibrium are shown in Figure 1.

SXL, and drive entrainment (Figure 3), whereas periods of up-front wind (when the winds are opposite to the geostrophic frontal jet) increase the surface buoyancy in the front, shoal the SXL, and drive detrainment. In the real ocean, the *EBF* sometimes vacillates in time between positive and negative values, primarily due to variations in the wind stress direction and amplitude, but also due to variations in the horizontal buoyancy gradient in the ocean $\nabla_h b$ [e.g., Thomas et al., 2015; Thompson et al., 2016]. Hence, a question arises: what is the time-integrated effect of these vacillations in the *EBF* (and wind stress more generally) on SXL depths, SXL nutrient budgets, and plankton ecosystems at a front?

In the real ocean, fronts are forced by both low-frequency and high-frequency winds [e.g., Alford, 2001; Gille, 2005]. High-frequency winds with variance near the local Coriolis frequency (i.e., near-inertial winds) resonantly excite near-inertial oscillations inside and outside fronts. The resonant response is peaked around the effective Coriolis frequency,

$$f_e = \left[f \left(f - \frac{\partial u}{\partial y} \right) \right]^{1/2}, \quad (3)$$

which depends on the Coriolis frequency as well as the local (in y) vertical relative vorticity of the frontal jet at the ocean surface (i.e., $-\partial u/\partial y$, see Figure 3) [e.g., Weller, 1982; Klein et al., 2004; Whitt and Thomas, 2015]. Due to the resonant amplification of near-inertial ocean currents by near-inertial winds at frequencies near f_e , near-inertial currents represent a large part of the surface ocean kinetic energy [e.g., Pollard and Millard, 1970; D'Asaro et al., 1995; Alford, 2001; Elipot and Lumpkin, 2008; Elipot et al., 2010]. In fact, there is a distinct peak in the kinetic energy spectrum of surface currents near the inertial frequency [e.g., Elipot and

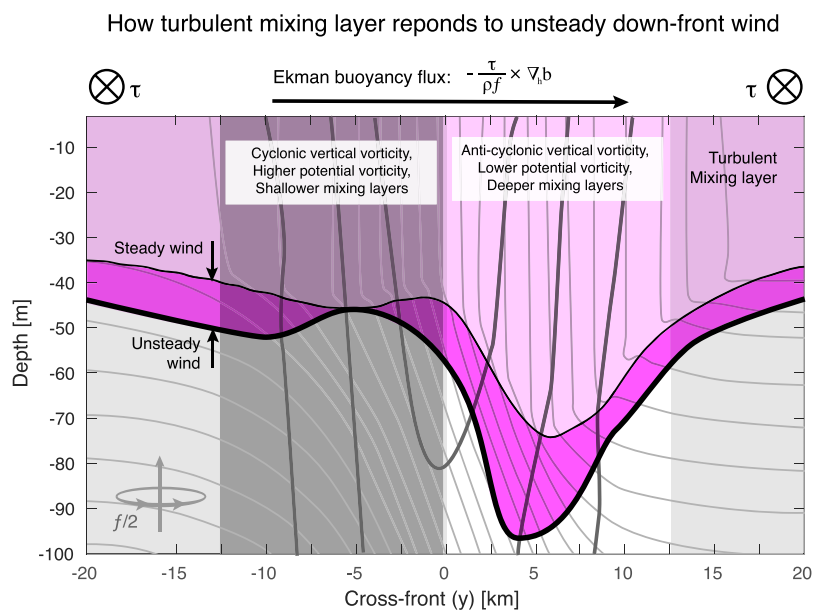


Figure 3. A schematic showing how the surface mixing layer (magenta) varies across an upper-ocean geostrophic front (thin gray lines denote isopycnals, thick darker gray lines denote isotachs of the along-front velocity u , which points into the page) under an unsteady down-front wind stress τ , which points in the direction of the frontal jet u (i.e., into the page). As the angular speed of rotation is positive, i.e., $f/2 > 0$ where f is the Coriolis frequency, there is an Ekman transport ($-\mathbf{k} \times \tau / \rho f$) to the right of the wind vector in the mixing layer, which induces an Ekman buoyancy flux ($-\tau / \rho f \times \nabla_h b$) that increases the surface density, reduces the vertical gradient of density (i.e., stratification) just below the mixing layer, and facilitates deeper wind mixing in the front. The mixing layers are deeper on the less dense side of the front due to anti-cyclonic vertical vorticity there (i.e., $-\partial u / \partial y < 0$), which is associated with lower values of Ertel's potential vorticity in the pycnocline (i.e., q , defined in section 1.1.3) and subinertial internal waves generated by the high-frequency part of the wind. See section 1.1.3.

Lumpkin, 2008], which is consistent with the long-held notion that near-inertial frequency winds make an outsized contribution (relative to the amplitude of the near-inertial stress) to mixed layer deepening and nutrient entrainment outside fronts [e.g., Price, 1981; Klein and Coste, 1984; D'Asaro, 1985b; Large et al., 1986; Crawford and Large, 1996; Jochum et al., 2013; Rodgers et al., 2014; Rumyantseva et al., 2015]. Moreover, inertial oscillations may open or amplify energy pathways from the geostrophic frontal jet to dissipation in the SXL [e.g., Whitt and Thomas, 2015; Thomas et al., 2015; Grisouard and Thomas, 2016] and concentrate [e.g., Kunze, 1985; Klein et al., 2004; Whitt and Thomas, 2013; Danioux et al., 2015; Pallàs-Sanz et al., 2016] and dissipate [e.g., Kunze et al., 1995; Inoue et al., 2010] in regions of anti-cyclonic vorticity (i.e., on the less dense side of the front shown in Figure 3). In addition, the flux of wind energy into near-inertial motions may be larger on the less dense side of the front, where f_e is lower, because the wind stress frequency spectrum has more variance at frequencies lower than f compared to frequencies greater than f (i.e., the stress has a red power spectrum) [e.g., Alford, 2001; Gille, 2005; Zhai, 2015]. Hence, near-inertial motions may have an even stronger effect on surface mixing in fronts than elsewhere [e.g., Lévy et al., 2009].

In summary, deepening of the SXL at a front depends on the magnitude, frequency content, and direction of the wind stress, as well as the Coriolis frequency. In addition, deepening of the SXL at a front depends on the horizontal buoyancy gradient and vertical vorticity at the ocean surface, as well as the potential vorticity at the top of the pycnocline [see (2)]; all three vary across a front [e.g., Pollard and Regier, 1992; Rudnick and Luyten, 1996] and are therefore important sources of spatial variability in the entrainment response to wind forcing at a front (as shown in Figure 3). Here numerical simulations will provide some examples showing how low-frequency and high-frequency oscillatory winds modify entrainment across a front.

1.2. Question and Outline

The question to be addressed in this manuscript is: how do oscillatory winds in general, and combined low-frequency and high-frequency winds in particular, modify phytoplankton at fronts? We address this question with output from a series of simulations of an idealized front forced by different combinations of oscillatory winds. Insight into the underlying physical and biogeochemical dynamics driving the phytoplankton

response will be derived from an analysis of phytoplankton distributions, phytoplankton growth and grazing loss rates, as well as SXL depths, nutricline depths, and the rate of nutrient entrainment into the SXL.

The outline of the remainder of the manuscript is as follows. Section 2 describes the numerical model configuration, the different wind forcing scenarios, and the metrics to be used in the analysis of the numerical experiments. The results in section 3 begin with a description of the spatiotemporal evolution of physics and biogeochemistry in an example simulation forced by combined low-frequency and high-frequency wind (section 3.1) and then discuss the physical and biogeochemical causes of the phytoplankton response to oscillatory wind at a front (sections 3.2–3.4). The article is concluded with a summary and discussion of the key results in section 4.

2. Experimental Setup

2.1. Model Configuration

The experiments are composed of a series of simulations of upper-ocean fronts forced by different oscillatory surface wind stresses. In order to isolate the dynamics associated with the low-frequency and high-frequency parts of the oscillatory wind in these experiments, the wind stress is purely oscillatory (unlike *Franks and Walstad* [1997], *Mahadevan et al.* [2008], and *Lévy et al.* [2009]), there are no spatial gradients in the applied wind stress $\partial\tau/\partial y=0$ [unlike *Martin and Richards*, 2001], no direct influence of boundaries [unlike *Spitz et al.*, 2003; *Siedlecki et al.*, 2011], no large scale velocity field that deforms the front [unlike *Mahadevan et al.*, 2008; *Lévy et al.*, 2009; *Mahadevan et al.*, 2010], and no surface buoyancy flux. Moreover, although all three components of the velocity are retained, all of the model variables are uniform in the along-front direction $\partial/\partial x=0$ and variability is only permitted in the vertical z and cross-front y directions. Hence, there are no three-dimensional mixed-layer baroclinic instabilities [unlike *Mahadevan et al.*, 2010], and the wind is oriented parallel to the frontal jet in all but one sensitivity experiment [unlike *Mahadevan et al.*, 2008; *Lévy et al.*, 2009; *Mahadevan et al.*, 2010]. Due to these simplifications, this work represents a first step toward understanding the effect of oscillatory winds on anomalously deep SXLs, nutrient entrainment and phytoplankton at fronts in nutrient-limited open-ocean conditions.

The model domain is horizontally periodic (in x and y) and bounded by a flat bottom at $z = -1000$ m and a free surface at $z \approx 0$ m. The physical initial condition consists of a pair of surface-intensified 30 km wide and 400 m deep frontal jets (Figure 4a) that are in geostrophic and thermal wind balance and spatially separated in the cross-front direction by roughly one jet width, which is about twice the mode-one baroclinic Rossby radius of deformation $NH/\pi f \approx 15$ km [e.g., *Gill*, 1982], where $N = .0045 \text{ s}^{-1}$ is the background

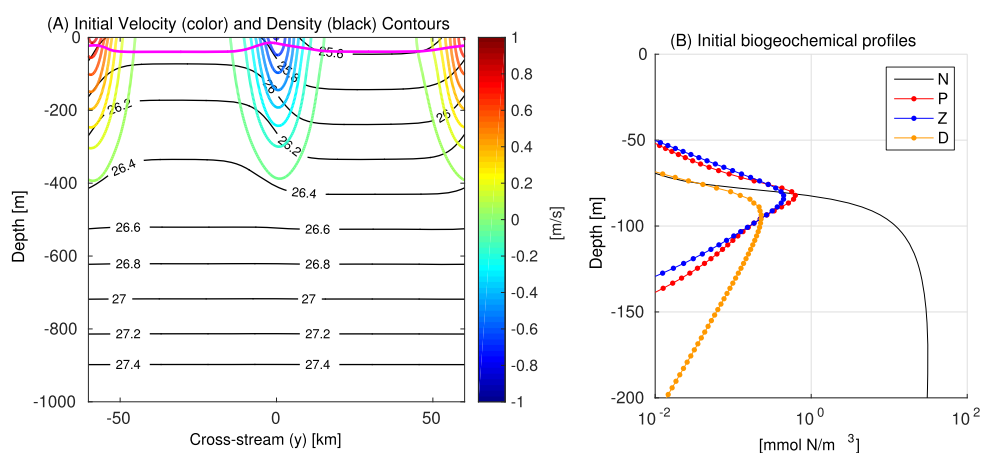


Figure 4. The initial conditions for (a) the physical model and (b) the biogeochemical model. The along-front velocity (colorbar) is in thermal wind balance with the density (thin black lines). A free surface displacement (not shown) cancels the baroclinic pressure gradient leading to a level of no motion at the bottom. The surface mixing layer depth H_s (magenta line), defined by the KPP vertical mixing parameterization, is averaged over the first 3 h of one simulation, when the along-front stress is approximately constant at $\tau_x = .18 \text{ N/m}^2$. The initial phytoplankton, zooplankton, detritus, and nutrient (P, Z, D, and N, respectively) are horizontally uniform. The initial vertical profiles in Figure 4b were derived from a 10 year simulation of a motionless diffusive vertical column initialized with $N = 14$, $P = 2$, $Z = 2$, $D = 2 \text{ mmol N/m}^3$, and $K_z = 2 \times 10^{-5} \text{ m}^2/\text{s}$. See section 2.1.

constant buoyancy frequency, $H = 1000$ m is the depth of the domain, and the Coriolis frequency $f = 10^{-4} \text{ s}^{-1}$. As the potential vorticity is initially positive, the initial condition is stable to all inviscid small disturbances (by the criteria of Hoskins [1974]). The ecosystem is initially horizontally uniform across the front—nutrient deplete at the surface and nutrient replete at depth—in a one-dimensional sinking-diffusion equilibrium with an SPM (Figure 4b) [e.g., Beckmann and Hense, 2007; Cullen, 2015].

Neither the physics nor the biogeochemistry are tuned to represent a particular set of observations, a particular oceanic province, or a particular season. The model is configured to be representative of an idealized open-ocean with isolated fronts, which are highly anisotropic features with strong cross-front gradients and weak along-front gradients by definition [e.g., Fedorov, 1986]. In the numerical experiments presented here the fronts have $\mathcal{O}(0.01)$ isopycnal slopes s_b just below the SXL base, $\mathcal{O}(1)$ SXL Rossby numbers $Ro = U/fL_J$ (where $U \approx 0.8$ m/s and $L_J \approx 15$ km are the characteristic velocity and half-width of the frontal jet, respectively), and small SXL depth H_s to frontal depth H_f ratios (here $H_s/H_f \approx 0.1$; see Figure 4a). This region of $(Ro, s_b, H_s/H_f)$ parameter space that we have chosen to characterize the physics in these simulations occurs at a wide range of horizontal length scales in midlatitude oceans, from about 100 to 200 km [e.g., Joyce et al., 2013] down to a few km [e.g., Lee et al., 2006], which include parts of what one might call the mesoscale and submesoscale. Hence, the results are applicable to fronts with horizontal length scales ranging from 1–100 km in the ocean to the extent that Ro , s_b , and H_s/H_f are not too dissimilar from those chosen here.

The biogeochemical model is configured to be representative of an idealized ocean where phytoplankton growth at the surface is limited by the availability of nutrients found at depth and phytoplankton growth at depth is limited by the availability of light found at the surface (i.e., nutrient-limited conditions); hence, phytoplankton are initially concentrated at an SPM where both light and nutrients are available. SPMs have been observed in a wide range of oceanic provinces, from upwelling regions and boundary currents to gyres, from the tropics to the poles, in regions with and without prominent spring blooms, inside and outside fronts, and at different times throughout the year, and their properties vary from place to place [e.g., Hitchcock et al., 1993; Claustre et al., 1994; Fernández and Pingree, 1996; Allen et al., 2005; Li et al., 2012; Cullen, 2015]. In the NPZD model, the attenuation of light with depth is the primary factor setting the depth of the SPM; the chosen light parameters (see supporting information Table S1) yield an SPM depth of about 75 m (see Figure 4b) that is within the range of observations in the open-ocean [e.g., Beckmann and Hense, 2007; Cullen, 2015]. See the supplement for more details about the biogeochemical model configuration [Franks et al., 1986; Steele and Henderson, 1992; Edwards and Brindley, 1999; Edwards and Yool, 2000].

Both the physics and ecosystem models are stepped forward in time using the regional ocean modeling system (ROMS) [Smolarkiewicz and Margolin, 1998; Shchepetkin and McWilliams, 2005]. Under wind forcing, vertical mixing is parameterized with the K-profile parameterization (KPP) scheme of Large et al. [1994] and explicit horizontal mixing of biogeochemical tracers is set to zero. Frequent reference is made to the SXL depth H_s , which is a diagnostic output of the KPP mixing model and represents a surface layer of elevated vertical diffusivity K_z and viscosity (see the supplement and Large et al. [1994] for more details). However, in order to isolate the effects of wind-driven variable vertical mixing on the biogeochemistry, some experiments (labeled CM for constant mixing) are run with a constant low vertical diffusivity $K_z = 2 \times 10^{-5} \text{ m}^2/\text{s}$ applied to biogeochemical tracers. Yet, in all the simulations, density and momentum are mixed with the variable vertical diffusivity and viscosity from KPP, hence the indirect effects of the wind-driven vertical mixing of momentum and density—that is the advective effects of the wind forcing—are present in all the simulation results discussed in this manuscript.

Each CM simulation is presented in comparison with an identical simulation with KPP mixing of biogeochemical tracers in order to separate the direct biogeochemical impacts of the wind-driven KPP mixing of the biogeochemical constituents from the indirect biogeochemical impacts of the wind forcing. The indirect impacts are dominated by vertical advection of biogeochemical constituents, which is induced by both the surface stress boundary condition and the KPP mixing of density and momentum. Hence, if the CM scenario is *similar* to the associated KPP mixing scenario, we infer that explicit wind-driven variable vertical mixing of biogeochemical tracers is *not* crucial for driving the biogeochemical response to the wind. On the other hand, if the CM scenario *differs* significantly from the associated KPP mixing scenario, we infer that explicit wind-driven variable vertical mixing of biogeochemical tracers *is* crucial for driving the biogeochemical response to the wind.

Details necessary to reconstruct the initial condition as well as further discussion of the model configuration can be found in WTL and the supporting information here. Additionally, some grid resolution sensitivity experiments are presented in the supporting information; our conclusions do not change on a finer computational grid.

2.2. Wind Forcing

Wind stresses in the real ocean contain all frequencies (example spectra can be found in *Alford [2001], Gille [2005], and Zhai [2015]*). However, the frequency spectrum of the surface ocean kinetic energy exhibits a spectral gap between low-frequency (subinertial) motions and high-frequency (near-inertial) motions in the midlatitudes [e.g., *Elipot and Lumpkin, 2008*]. Hence, we regard unsteady wind-forced motions as being dominated by two distinct frequency bands: (1) low-frequency (LF) unsteady Ekman flows, which are forced primarily by synoptic and planetary-scale atmospheric variability with forcing frequencies $\omega^L \ll f$ and (2) high-frequency (HF) near-inertial motions, which are forced by atmospheric variability with frequencies $\omega^H \approx f$ [e.g., *Pollard and Millard, 1970; D'Asaro, 1985a; Alford, 2001*].

Here we focus on how phytoplankton at a front respond to changes in nutrient entrainment induced by the combination of LF and HF stresses. For comparison, we also examine the response to only high and only low frequency forcing. As in WTL, the model experiments are forced by spatially uniform but time-dependent wind stresses defined as cosine functions of time so that the average of the time-integrated Ekman buoyancy flux [see (1) and (2)] over an LF forcing period is approximately zero, that is

$$\frac{1}{T} \int_0^T \int_0^t EBF(s); ds dt \approx 0., \tag{4}$$

where s and t are time-integration variables and T is the length of one low-frequency wind forcing period (i.e., 8 days). Here we present results of a simulation forced by combined LF and HF oscillatory along-front wind stress, labeled LFHF, and defined by $\tau_x(t) = \tau^L(t) + \tau^H(t)$ where the low-frequency wind is composed of a single frequency, $\tau^L = .18 \cos(.09ft)$ N/m² (an 8 day period), and the high-frequency wind is composed of multiple frequencies, $\tau^H = \sum_{i=1}^{11} .02 \cos(\omega_i^H t + \phi_i)$ N/m², which are evenly spaced from $\omega_1^H = .45f$ to $\omega_{11}^H = 1.45f$ around the local Coriolis frequency $f = 10^{-4} \text{ s}^{-1}$, that is the high-frequency forcing periods range from 1.6 to 0.5 days, the phases ϕ_i are random and uniformly distributed from 0 to 2π , and the cross-front wind stress $\tau_y = 0$.

To elucidate the biogeochemical implications of combined LFHF forcing, explicit comparisons are made between the primary LFHF scenario and simulations forced by either the LF or HF part of the wind alone (sections 3.2 and 3.3). Furthermore, results from a series of sensitivity experiments are presented (section 3.4) to emphasize how the results depend on the orientation of the wind relative to the front and the particular high frequencies ω^H . See Table 1 for a concise list of all the simulations and section 4 of the supporting information for a description of all the simulations in one place.

Table 1. List of All Simulations Referred to in This Manuscript^a

Label	Surface Stress Function	Mixing	Grid (y × z)	Orient
1. LFHF	$.18 \cos(.09ft) + \sum_{i=1}^{11} .02 \cos(\omega_i^H t + \phi_i)$	KPP	400 × 200	
2. LF	$.18 \cos(.09ft)$	KPP	400 × 200	
3. HF	$\sum_{i=1}^{11} .02 \cos(\omega_i^H t + \phi_i)$	KPP	400 × 200	
4. LFHF CM	$.18 \cos(.09ft) + \sum_{i=1}^{11} .02 \cos(\omega_i^H t + \phi_i)$	$K_z = 2 \times 10^{-5}$	400 × 200	
5. LF CM	$.18 \cos(.09ft)$	$K_z = 2 \times 10^{-5}$	400 × 200	
6. HF CM	$\sum_{i=1}^{11} .02 \cos(\omega_i^H t + \phi_i)$	$K_z = 2 \times 10^{-5}$	400 × 200	
7. LF S	$.12 \cos(.09ft)$	KPP	400 × 200	
8. LFHF S0.3f	$.12 \cos(.09ft) + .06 \cos(.3ft)$	KPP	400 × 200	
9. LFHF S0.8f	$.12 \cos(.09ft) + .06 \cos(.8ft)$	KPP	400 × 200	
10. LFHF S1.2f	$.12 \cos(.09ft) + .06 \cos(1.2ft)$	KPP	400 × 200	
11. LFHF S2.0f	$.12 \cos(.09ft) + .06 \cos(2.0ft)$	KPP	400 × 200	
12. LFHF Y S0.8f	$.12 \cos(.09ft) + .06 \cos(.8ft)$	KPP	400 × 200	cross-front
13. LFHF 8 × 4	$.18 \cos(.09ft) + \sum_{i=1}^{11} .02 \cos(\omega_i^H t + \phi_i)$	KPP	800 × 400	
14. LF 8 × 4	$.18 \cos(.09ft)$	KPP	800 × 400	

^aThe surface stress is in N/m² and K_z is in m²/s. The third column indicates the vertical diffusivity applied to the biogeochemical tracers, which is equal to a constant in the scenarios labeled CM or equal to the variable diffusivity of density determined by the KPP scheme. Experiments 13 and 14 are identical to 1 and 2, respectively, except that the grid resolution has been doubled. All of the wind stresses are oriented along the front except 12, which is oriented in the cross-front direction. The conclusions of this manuscript do not change on the finer grid; see supporting information Figure S1.

2.3. Metrics

This section describes the metrics used to show how nutrients and phytoplankton respond to wind forcing in the simulations. Metrics include the phytoplankton concentrations (P), full-depth-integrated phytoplankton biomass ($P_{int} = \int_{z=-H}^0 P dz$ where $H = 1000$ m is the domain depth), and nutricline depths ($H_{N=15}$, where the $N = 15$ mmol N/m³ isopleth is used as a proxy for the nutricline). In addition, the depth-integrated phytoplankton growth rates (section 2.3.1) and depth-integrated phytoplankton loss rates due to grazing (section 2.3.2) give insight into the biological mechanisms (increased nutrient uptake and/or reduced grazing) that drives the changes in phytoplankton under wind forcing. Finally, the rate of nutrient entrainment into the SXL (section 2.3.3) encapsulates the direct effects of wind-driven surface mixing on vertical nutrient fluxes in nutrient-limited oceans.

2.3.1. Phytoplankton Growth: Primary Production

Phytoplankton growth near the surface is limited by low nutrient concentrations in these experiments. Hence, wind-driven upward nutrient fluxes can fuel phytoplankton growth via nutrient uptake (i.e., primary production). In this ecosystem model, primary production is constrained by light, nutrients, and the phytoplankton concentration, that is

$$UP = \frac{V_m N}{k_N + N} \frac{\alpha I}{\sqrt{V_m^2 + \alpha^2 I^2}} P, \quad (5)$$

where the maximum phytoplankton growth rate is $V_m = 1.0$ d⁻¹, I is the photosynthetically available radiation, $\alpha = .15$ d⁻¹ (W/m²)⁻¹ is the initial slope of the productivity-irradiance curve, and $k_N = 0.1$ mmol N/m³ is the nutrient half-saturation constant. See the supporting information for details.

2.3.2. Phytoplankton Losses: Senescence and Grazing

Phytoplankton losses are due to senescence, that is $-\sigma_d P$ where the senescence rate $\sigma_d = .03$ d⁻¹, and zooplankton grazing, that is

$$GZ = R_m (1 - \exp(-\Lambda P)) Z, \quad (6)$$

where the maximum zooplankton grazing rate $R_m = 0.5$ d⁻¹, and the Ivlev parameter $\Lambda = 1.5$ (mmol N/m³)⁻¹. See the supporting information for details.

2.3.3. Vertical Nutrient Fluxes

Primary production (5) is facilitated by upward nutrient fluxes, due to either advection or mixing. Rather than explicitly plot advective and diffusive nutrient fluxes at fixed locations in space—as discussed in WTL, such a decomposition can lead to incorrect conclusions about the dynamical mechanism leading to the net nutrient transport in flows dominated by oscillations—we separate the effects of advection from explicit wind mixing on biogeochemistry in these experiments by comparing simulations that are identical except for the vertical diffusivity of biogeochemical tracers, as discussed in section 2.1.

In the default KPP-mixing simulations, the vertical diffusivities are generally small $K_z \sim 10^{-5}$ m²/s below the wind-driven SXL and large $K_z \sim 10^{-2}$ m²/s in the wind-driven SXL. In this case, the flux of nutrients across the base of the SXL is of primary importance. Hence, the effect of wind-driven vertical mixing on vertical nutrient fluxes is quantified using an entrainment flux [e.g., *De Szoeke, 1980; Stevenson and Niiler, 1983*]. The nutrient entrainment flux is defined relative to the SXL base H_s , which is defined by the KPP mixing scheme based on the bulk Richardson number (as in *Large et al. [1994]*) and separates the region of direct and strong wind-driven vertical mixing (above H_s) from weak interior mixing driven only by local velocity shears (below H_s).

The SXL base H_s (defined so that $H_s < 0$) moves with a vertical velocity

$$w^* = \frac{\partial H_s}{\partial t} + v(H_s) \frac{\partial H_s}{\partial y} - w(H_s), \quad (7)$$

relative to a material surface, which moves with the fluid velocity. Positive w^* indicates the SXL base is moving toward shallower depths relative to the material surface (fluid is detrained from the SXL) and negative w^* indicates the SXL base is moving toward deeper depths relative to the material surface (fluid is entrained into the SXL).

Then, the entrainment flux of nutrient across the SXL base is:

$$\mathcal{F} = w^* [\bar{N} - N(H_s)], \quad (8)$$

where $\bar{N} = \frac{1}{|H_s|} \int_{H_s}^0 N dz$ is the average nutrient concentration in the SXL and $N(H_s)$ is the nutrient concentration at the SXL base. The flux \mathcal{F} is called an entrainment flux when $\mathcal{F} \geq 0$ (generally when w^* is negative in these simulations) and a subduction flux when $\mathcal{F} < 0$ (generally when w^* is positive in these simulations) [e.g., Cushman-Roisin, 1987].

When plotting \mathcal{F} , we only present the positive part $\mathcal{F} \geq 0$, that is the entrainment flux of nutrient into the SXL, because entrained nutrients are rapidly and irreversibly homogenized throughout the SXL. Moreover, even if the SXL subsequently shoals to the surface before the nutrient is consumed, the biogeochemical impact of the redistributed nutrient will persist. Finally, we filter the inherently noisy entrainment flux with a 1 day moving average filter before plotting to reduce oscillations associated with near-inertial motions.

3. Results

The results are organized as follows: section 3.1 contains a qualitative description of the time evolution of phytoplankton in the front during the first 18 days of combined LFHF wind. To clarify how the low-frequency and high-frequency parts of the wind contribute to the phytoplankton response, section 3.2 compares the phytoplankton responses under only LF, only HF, and combined LFHF winds. Then, by comparing the LF, HF, and LFHF simulations with the analog simulations where the effects of wind-driven mixing of biogeochemical tracers are removed (i.e., the CM scenarios; see Table 1 and section 2.1), section 3.3 identifies where and to what degree wind-driven mixing and advection contribute to changes in phytoplankton under LF, HF, and LFHF wind. Finally, section 3.4 presents the results of some additional sensitivity studies, which show how the synergistic biogeochemical response to LFHF wind at a front depends on (1) the particular near-inertial frequency components in the HF wind and (2) the along-front (as opposed to the cross-front) component of the LF wind and the associated *EBF*. In particular, the sensitivity experiments are designed to show that the synergistic biogeochemical response to LFHF wind at the front is not merely due to the increased amplitude of the LFHF stress relative to the LF or HF stress acting alone.

3.1. Time Evolution Under Combined Low-Frequency and High-Frequency Wind

Here the effect of oscillatory winds on phytoplankton at a front is demonstrated with a specific numerical example. In particular, this section contains a qualitative description of the time evolution of some key physical and biogeochemical variables during the first 18 days of the LFHF wind, when the cross-front averaged P_{int} exhibits the most rapid secular growth (Figure 5c). The description refers frequently to Figure 6, which contains 8 cross-front (y, z) sections of the density, along-front velocity u , SXL depth H_s , nutricline depth $H_{N=15}$ (defined in section 2.3), and phytoplankton concentration P , all in the front centered at $y = 0$ in Figure 4a. The wind stress time series is plotted as a black line in Figure 5a.

At the initial time, the wind is pointed up-front ($\tau_x > 0$, i.e., out of the page in Figure 6), which results in a negative Ekman buoyancy flux [*EBF*, defined in (1)] and a period of increasing surface buoyancy and stratification in the front until the wind stress reverses direction at $t = 2$ days and ultimately reaches its maximum amplitude in the down-front direction at day 4 (Figure 6a), when the *EBF* is approximately maximum and $\int_{t=0}^{4d} EBF(s) ds \approx 0$ [see (2) and Figure 5b]. At this time, $EBF(t) = \max_t EBF(t) \approx 1.5 \times 10^{-7} \text{ m}^2/\text{s}^3$, where the horizontal buoyancy gradient in (1) is averaged from $y = -20$ to 20 km. For perspective, the equivalent heat flux is about $400 \text{ W}/\text{m}^2$. The main physical difference between day 4 and day 0 (in Figure 4) is a slightly deeper SXL and a pycnocline at the SXL base, which emerges due to the wind mixing [e.g., Pollard et al., 1972]. Both the nutricline and the SPM are displaced slightly in the vertical, but P_{int} has not changed significantly across the front (Figure 5c).

At day 6 (Figure 6b), surface densities are significantly higher across the front than at day 4 or day 0, and the SXLs are significantly deeper, particularly on the less dense side of the front, despite the relatively small wind stress amplitude $|\tau|$. These deep SXLs occur when the time-integrated *EBF*, i.e., $\int_0^t EBF(s) ds$ (plotted in Figure 5b), reaches a local maximum in time t , consistent with the theory in section 1.1 and Figure 3. To put the effect of this time-integrated *EBF* in perspective, the magnitude of $\int_{t=0}^{6d} EBF(s) ds \approx 0.017 \text{ m}^2/\text{s}^2$ is approximately equivalent to a change in the depth-integrated ocean heat content of $42 \text{ MJ}/\text{m}^2$, which is equivalent to an average heat loss of about $80 \text{ W}/\text{m}^2$ over 6 days (compare, for example, with observed upper-ocean heat content anomalies associated with eddies in the Drake passage

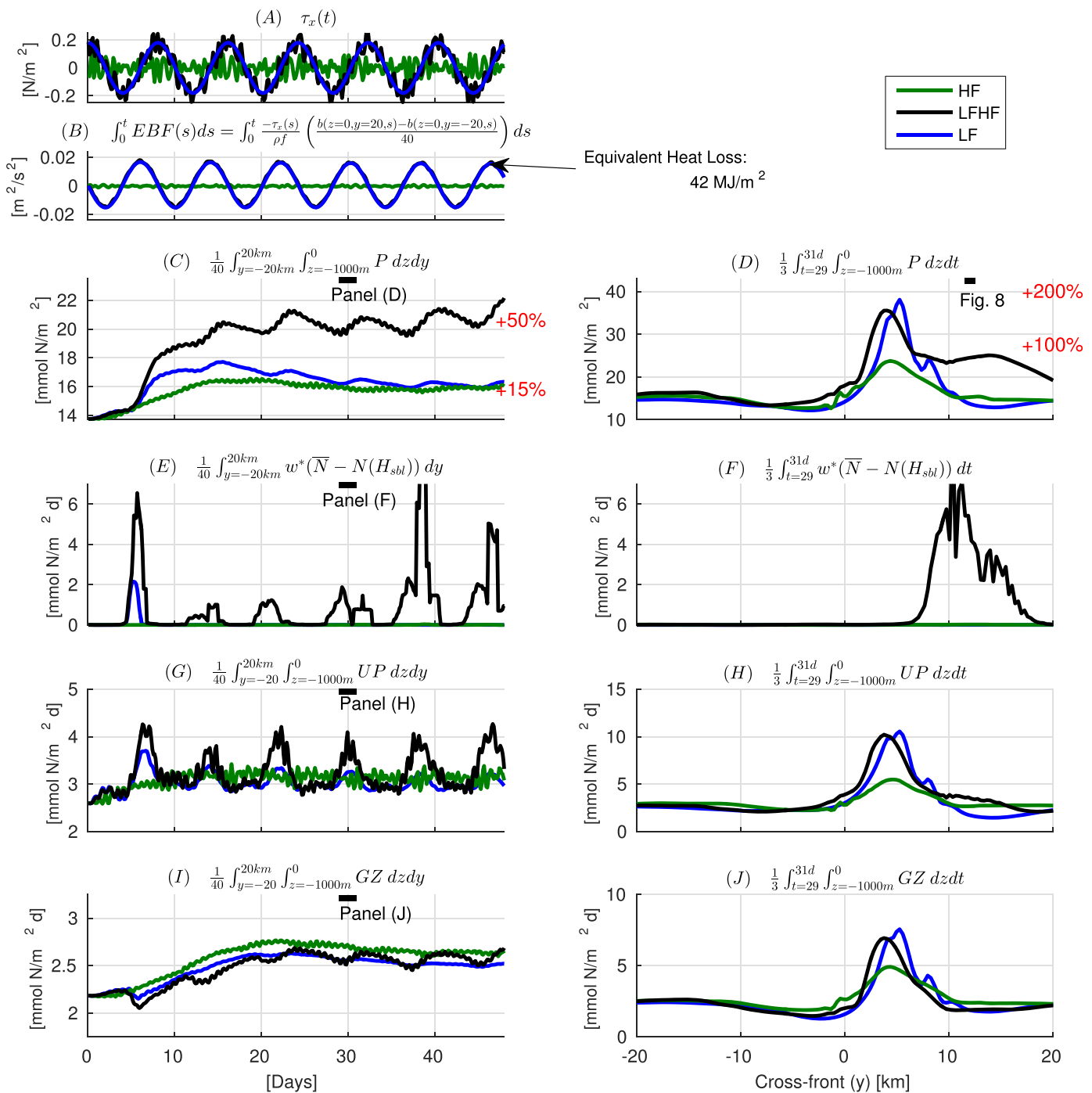


Figure 5. (left) Time plots of cross-front-averages (from $y = -20$ to 20 km) and (right) cross-front plots of time-averages (from $t = 29$ to 31 days) from experiments forced by low frequency (LF, blue lines), high frequency (HF, green lines), and low frequency plus high frequency (LFHF, black lines) along-front wind. (A) The wind stress, $\tau_x(t)$; positive τ_x indicates up-front wind and negative Ekman buoyancy flux EBF [defined in (1)], whereas negative τ_x indicates down-front wind and positive EBF . (B) The time-integrated Ekman buoyancy flux $\int_0^t EBF(s) ds$ [see (2)]. Biogeochemical variables consist of: (C and D) full-depth-integrated phytoplankton $P_{int} = \int_{z=-1000}^0 P dz$, (E and F) nutrient entrainment flux into the surface mixing layer [see (8)], (G and H) full-depth-integrated primary production [see (5)], and (I and J) full-depth-integrated grazing rate [see (6)] (all of which are discussed in section 2.3). The 3 day time averages in the right column are centered on day 30 so that they coincide with a local maximum in time-integrated EBF , nutrient entrainment and primary production like days 6 and 14 in Figure 6 but during the fourth LF forcing period, when full-depth-integrated biogeochemical quantities are less-variable from one LF forcing period to the next.

[Stephenson et al., 2013]). Largely as a result of the reduced stratification and deeper SXLs arising from the time-integrated EBF , phytoplankton as well as nutrients (Figure 5e) have been entrained into the SXL between about $y = 3$ and 10 km.

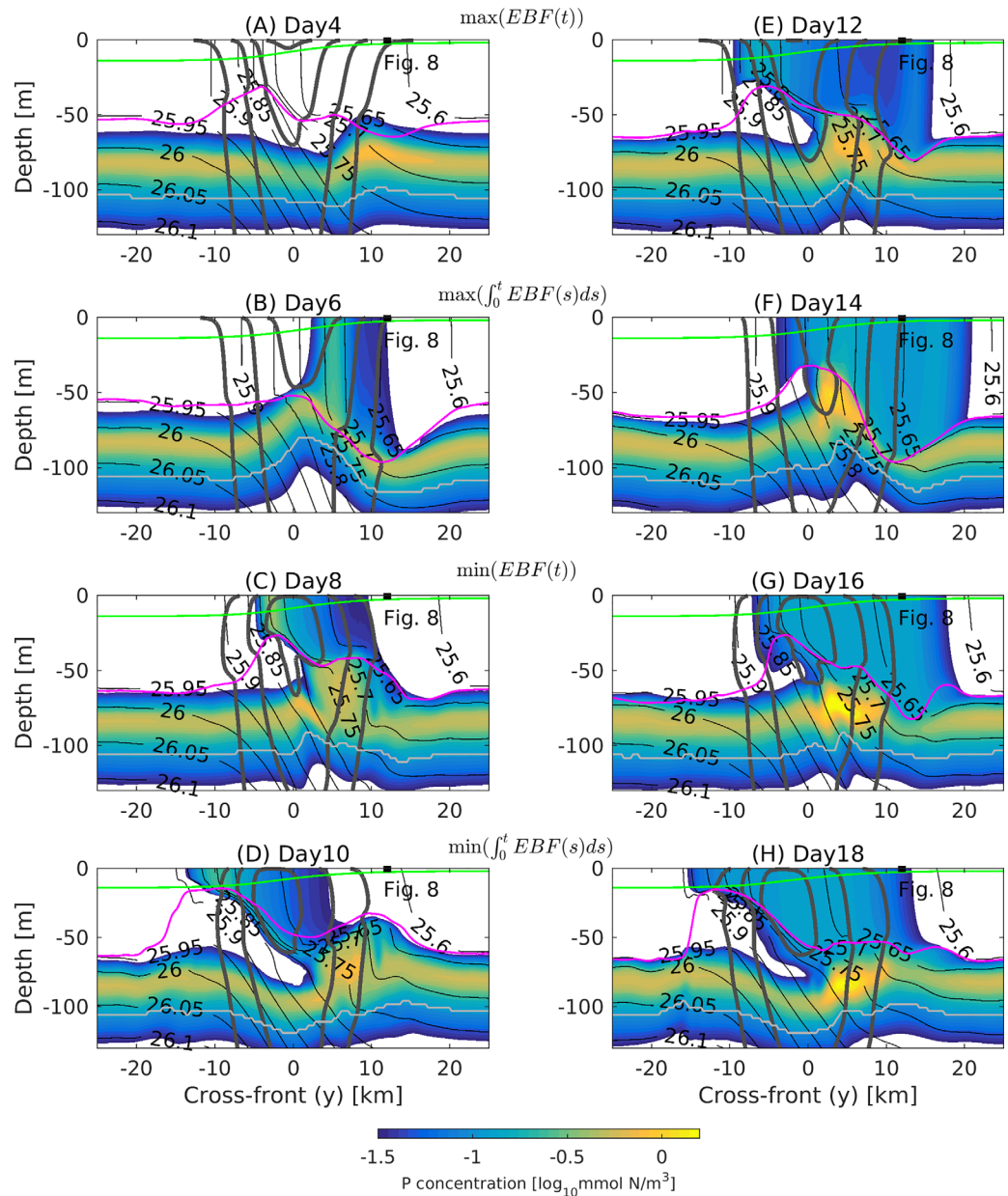


Figure 6. A series of snapshots from the primary simulation forced by combined low-frequency and high-frequency (LFHF) oscillatory along-front wind. The wind stress $\tau_x(t)$ is plotted in black in Figure 5a. Phytoplankton concentration (P in mmol N/m^3 , color), isopycnals (thin black lines every 0.05 kg/m^3), KPP-defined mixing layer depth (i.e., H_s , magenta lines), the nutricline depth (thin light gray lines denote the $N = 15 \text{ mmol N/m}^3$ isopleth depth $H_{N=15}$, which is a proxy for the nutricline depth), and isotachs of the along-front velocity u (thick dark gray lines every 0.2 m/s). The free surface displacement (multiplied by 100 for clarity) is plotted as a green line just below the surface. The phase of the oscillatory LF wind is the same in each row: the top row is associated with a maximum in down-front wind stress, hence a maximum in the Ekman buoyancy flux, $EBF(t) = -\frac{\tau_x}{\rho} \frac{\partial \rho}{\partial y}$, the second row with zero wind stress and a maximum in the time-integrated Ekman buoyancy flux, $\int_0^t EBF(s) ds$, the third row with a maximum in up-front wind, hence a minimum in $EBF(t)$, and the fourth row with zero wind stress and a minimum in $\int_0^t EBF(s) ds$. The time-integrated EBF is plotted in Figure 5b. “Mooring plots” at $y = 12 \text{ km}$ can be found in Figure 8d. See section 3.1.

At day 8 (Figure 6c), the winds are at their maximum up-front amplitude again and the EBF is minimum (like day 0). The front has restratified relative to day 6, and the SXL has shoaled in the vicinity of the front despite the large $|\tau|$. The stratification and phytoplankton concentrations have changed relative to the initial condition. In particular, there is a thin but highly stratified layer just below the SXL base in the front that overlies a thicker more weakly stratified layer, which extends roughly from the sharp pycnocline at the SXL base to the deepest SXL depths that occurred on day 6. Between about $y = 3$ and 12 km , approximately where the

SXL reached the SPM on day 6, this weakly stratified layer is associated with higher phytoplankton concentrations and a thicker SPM.

At day 10 (Figure 6d), when $|\tau(t)|$, $|EBF(t)|$ and $\int_0^t EBF(s)ds$ all reach local minima in time, the phytoplankton in the SXL along with the outcropping isopycnals have been advected toward the dense side of the front by the Ekman flow. The increase in frontal stratification due to the negative EBF from day 6 to day 10 is associated with an equivalent increase in ocean heat content of 85 MJ/m^2 over 4 days (which is approximately equivalent to a sustained heat flux of about 250 W/m^2 into the ocean for 4 days). The highly stratified layer below the SXL base is more strongly stratified than at day 8, and the phytoplankton concentration at the SPM has increased slightly between about $y = 3$ and $y = 10 \text{ km}$.

Days 12 to 18 (Figures 6e–6h) are analogous to days 4 to 10 (Figures 6a–6d)—they occur one LF forcing period later—so only differences will be highlighted. In particular, day 12 (Figure 6e) differs from day 4 (Figure 6a) in that the SXL is significantly deeper near $y = 12 \text{ km}$ and entrainment of phytoplankton has begun during the period of maximum down-front wind stress and maximum EBF . However, the maximum nutrient entrainment rate on the less dense side of the front still lags the maximum down-front wind stress (Figure 5e). In fact, nutrient entrainment on the less dense side of the front reaches a local maximum as wind stress magnitude $|\tau|$ drops toward zero near day 14 (Figures 5e and 6f), which is qualitatively consistent with the first LF forcing period and the theory in section 1.1 (see Figure 3). Note that the phytoplankton concentrations remain relatively low $P < 0.4 \text{ mmol N/m}^3$ in the SXL. Nevertheless, at day 14, phytoplankton now occupy a much wider region of the SXL in the front. In addition, at $y = 4 \text{ km}$, the phytoplankton concentration at the SPM increases throughout days 12–18 and remains persistently higher than SPM concentrations outside the front.

In summary, the oscillatory LFHF wind forcing causes large oscillatory LF deviations in the near-surface density and SXL depths, and therefore episodic nutrient entrainment into the SXL as well as secular wind-forcing-period-integrated changes to the phytoplankton distribution near the front. Prominent features of the forcing-period-integrated phytoplankton response to LFHF wind are:

1. Phytoplankton accumulate at high concentrations (i.e., $P > 0.4 \text{ mmol N/m}^3$) in the SPM near $y \approx 4 \text{ km}$.
2. Phytoplankton accumulate at low concentration (i.e., $P < 0.4 \text{ mmol N/m}^3$) in the SXL on most isopycnals that outcrop at the front.
3. SXLs are deepest and closest to the nutricline on the less dense side of the front at times near the local maxima in the time-integrated EBF (i.e., at days 6 and 14 in Figure 6), which lag the local maxima in down-front wind stress by 2 days. These times are associated with significant nutrient entrainment into the SXL (Figures 5e and 5f), vertical redistribution of phytoplankton in the SXL (Figure 6), enhanced depth-integrated phytoplankton growth rates (Figures 5g and 5h), and relatively low depth-integrated zooplankton grazing rates (Figures 5i and 5j), hence large phytoplankton accumulation rates (Figure 5c).

Before proceeding to the comparisons with other experiments, it is worth noting that the jet remains essentially stationary from day 4 to 18, although the surface density gets displaced by as much as 15 km across the front (Figure 6). The strong geostrophic momentum of the frontal jet does not get advected back and forth by the Ekman flow due to the cross-front pressure gradient force and the Coriolis force, both of which remain in rather tight geostrophic balance at all times in this scenario, where the strong pressure gradient force arises primarily from the gradient in the free surface, which is displayed in Figure 6.

3.2. Comparing the Phytoplankton Responses to Different Wind Frequencies

To separate the effects of low-frequency and high-frequency along-front winds on phytoplankton at the front, we compare the simulation forced by LFHF wind with simulations forced by LF or HF wind alone.

Snapshots of the phytoplankton concentration $P(y, z)$ across the front after 30 days of forcing (Figure 7) and time series of $P(z, t)$ on the less dense side of the front (Figure 8) highlight the qualitative differences and similarities between the three wind scenarios. The time of the snapshots is chosen to coincide with a local maximum in the time-integrated Ekman buoyancy flux $\int_0^t EBF(s)ds$ (introduced in (2) and plotted in Figure 5b) and deepest SXLs in an LF forcing period after the most rapid secular phytoplankton growth has subsided, that is after the first 24 days or so (see Figure 5c). Both the snapshots (Figure 7) and time series (Figure 8) show that the LFHF scenario differs from the other two scenarios in that the SXL intermittently reaches

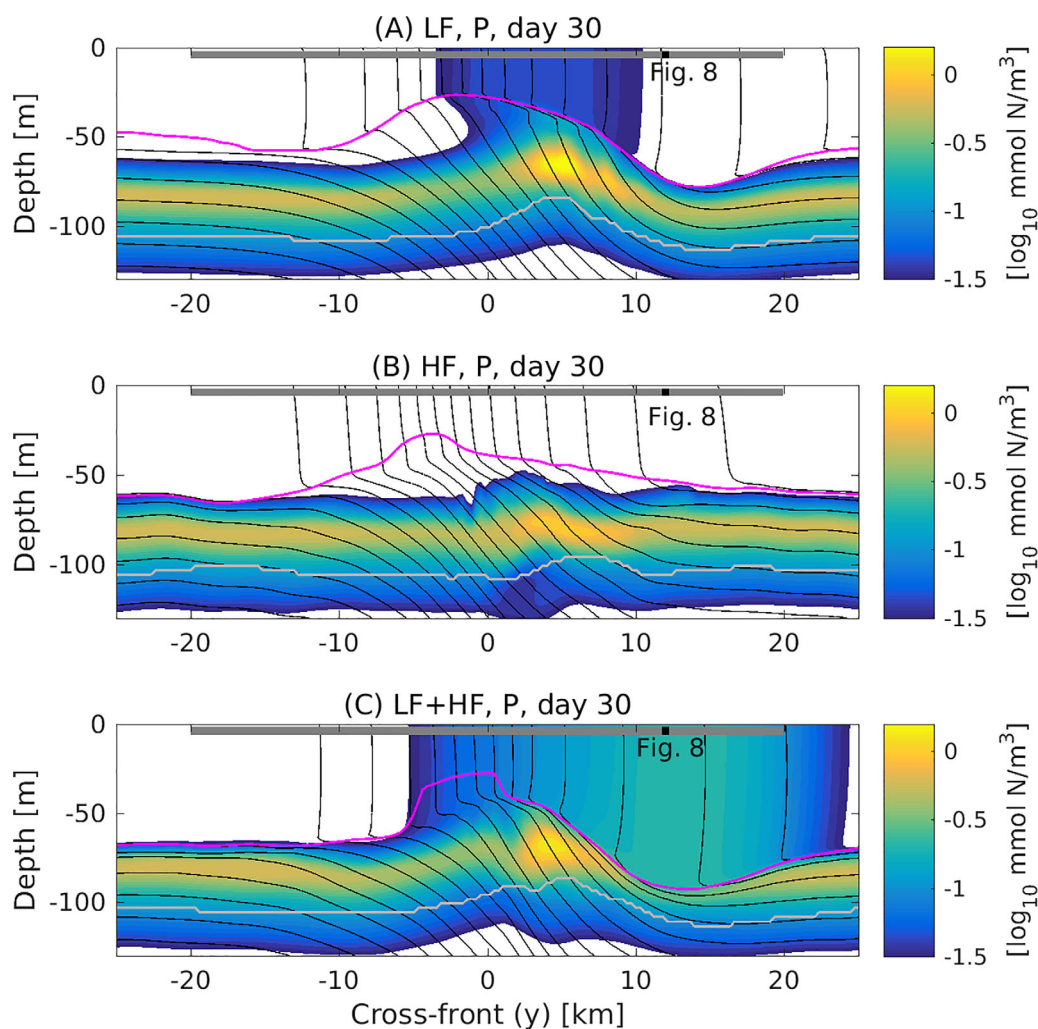


Figure 7. Snapshots of phytoplankton concentration $P(y, z)$ (color), density $\rho(y, z)$ (thin black lines every 0.025 kg/m^3), the $N = 15 \text{ mmol/m}^3$ isopleth depth $H_{N=15}(y)$ (gray line), and the KPP-defined surface mixing layer depth H_s (magenta line) at $t = 30$ days, which coincides with the center of the 3 day time averages in the right column of Figure 5. The gray bar at the surface indicates the cross-front averaging range ($y = -20$ to 20 km) used throughout the paper, whereas the black hashmark indicates the location ($y = 12 \text{ km}$) of the “mooring plots” in Figure 8 and histograms in Figure 10.

the SPM once every LF wind period (8 days). Hence, phytoplankton concentrations in the SXL are significantly greater under LFHF wind than under LF or HF wind. Yet, all three scenarios are similar in that the vertical phytoplankton distribution $P(z)$ outside the front is unmodified by the wind, the winds drive oscillatory vertical displacements of the SPM in the front with periods similar to the winds, and the SPM has higher phytoplankton concentrations at $y \approx 4 \text{ km}$ on the less dense side of the front.

More quantitative results are presented in Figure 5, where it is shown that P_{int} is elevated on the less dense side of the front in all three wind scenarios (Figure 5d). After the most rapid transient phytoplankton accumulation has subsided (i.e., after about 24 days or 3 LF forcing periods), the cross-front average (from $y = -20$ to 20 km) of P_{int} is elevated by 50% under LFHF wind and 15% under both LF and HF wind relative to the initial condition. Note, in contrast, that the cross-front average of P_{int} increases by less than 3% relative to the initial condition in a simulation without any wind forcing [WTL].

The maximum (in y) of P_{int} occurs at $y \approx 4 \text{ km}$ on the less dense side of the front in all three wind scenarios and varies from approximately 35 mmol N/m^2 under LF and LFHF wind to 25 mmol N/m^2 under HF wind (to 14 mmol N/m^2 outside the front, see Figure 5d). Although $\max_y P_{int}$ is significantly greater in the LF scenario than in the HF scenario, there is slightly more P_{int} at essentially all other y from -20 to 20 km in the HF scenario (Figure 5d), which explains why the cross-front average P_{int} is similar under LF and HF wind

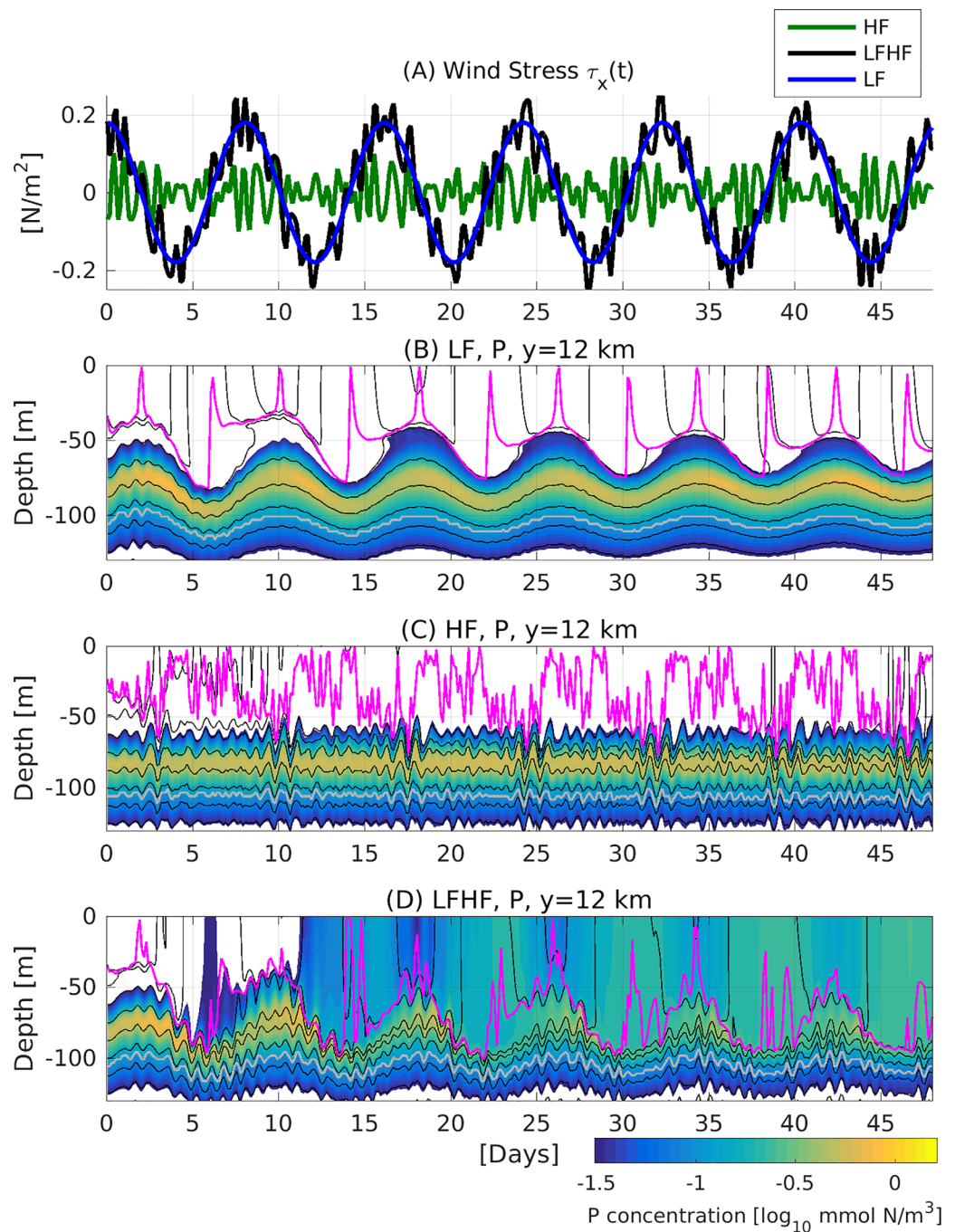


Figure 8. “Mooring plots” from experiments forced by (b) low frequency (LF), (c) high frequency (HF), and (d) low frequency plus high frequency (LFHF) along-front oscillatory wind stresses, which are plotted in (a) in blue, green, and black, respectively. Phytoplankton concentration (color), density (thin black contours every $.025 \text{ kg/m}^3$), the $N = 15 \text{ mmol/m}^3$ isopleth depth (gray line), and the KPP-defined surface mixing layer depth H_s (magenta line) are plotted at $y = 12 \text{ km}$, the same y location marked by black hash marks at $z = 0$ in Figure 7.

(Figure 5c). Similarly, although $\max_y P_{int}$ (at $y \approx 4 \text{ km}$) is similar in the LF and LFHF scenarios, P_{int} is higher at essentially all other y from -20 to 20 km in the LFHF scenario than in the LF (or HF) scenario (Figure 5d). In fact, the most striking difference between the LFHF scenario and either the LF or HF scenarios—the focus of this paper—occurs between $y \approx 10$ and 20 km , where P_{int} is elevated by about 100% relative to the initial condition and phytoplankton concentrations are elevated in the SXL under LFHF wind, but phytoplankton vertical profiles are essentially unchanged from the initial condition under HF or LF wind acting alone

(Figures 5d, 7, and 8). The question then becomes: what is the dynamical cause of this elevated phytoplankton in the SXL on the less dense side of the front in the LFHF scenario?

3.3. How Oscillatory Along-Front Winds Modify Phytoplankton at a Front

Changes in the cross-front-averaged and full-depth-integrated phytoplankton biomass $\frac{1}{40} \int_{y=-20}^{20} P_{int} dy$ (shown in Figure 5c) result almost entirely from the time-and-space-integrated imbalance between the growth rate [primary production, defined in (5)] and the loss rate [linear senescence plus zooplankton grazing, defined in section 2.3.2]. In particular, with the exception of horizontal transport across the frontal margins at $y = \pm 20$ km, which Figure 6 suggests is negligible, redistribution of P by advection and mixing has no direct effect on $\frac{1}{40} \int_{y=-20}^{20} P_{int} dy$. On the other hand, all of the biogeochemical changes due to the oscillatory wind are ultimately, albeit indirectly, attributable to wind-driven advection and mixing. In this section, we aim to identify how the advection and mixing driven by oscillatory wind modifies phytoplankton growth and grazing rates, and hence phytoplankton.

All the oscillatory wind scenarios induce both secular and oscillatory imbalances between growth and loss rates (Figures 5g–5j) due to the mismatch between the faster phytoplankton and slower zooplankton specific growth rates (which have maxima of $U_{max} = 1.0 \text{ d}^{-1}$ and $G_{max} = 0.5 \text{ d}^{-1}$, respectively; both U and G have average values of about 0.2 d^{-1} over the top 100 m in the simulations, not shown). The secular imbalance due to the onset of forcing—and the associated rapid increase in nutrient consumption in the euphotic zone (Figure 5g)—induces the forcing-period-averaged accumulation of P , which is most rapid at early times (that is during the first 24 days). Eventually zooplankton grazing increases to match the increased nutrient uptake rate (Figure 5i) and a cyclostationary balance is achieved. The oscillatory imbalances persist throughout the 48 days of wind forcing but do not lead to significant forcing-period-integrated changes in P after about 24 days (Figure 5c). The dynamical causes of the secular imbalances between growth and loss are discussed in the following two subsections, which refer to the regions where P rises in (section 3.3.1) the SPM at $y \approx 4$ km and in (section 3.3.2) the SXL at $y \approx 12$ km.

3.3.1. Enhanced Phytoplankton at the Subsurface Phytoplankton Maximum

WTL show that under LF wind the secular increase in P in the SPM at $y \approx 4$ km on the less dense side of the front arises primarily from: (1) oscillatory LF vertical displacements due to nonlinear Ekman pumping (defined as in Stern [1965]) and (2) a forcing-period averaged vertical circulation. The oscillatory Ekman pumping has a period of 8 days, vertical velocities of about 10 m/d, and peak-to-trough vertical displacements of about 25 m, which induce transient vertical displacements of the SPM and nutricline (e.g., from day 14 to day 18 at $y \approx 4$ in Figure 6). The onset of oscillatory Ekman pumping causes P concentrations to increase at the SPM during the first few LF forcing periods, but Ekman pumping is not responsible for the sustained increase in P over multiple forcing periods [WTL]. Instead, the time-mean vertical velocity of about 0.2 m/d drives an advective nutrient flux to the SPM that maintains a higher P concentration at $y \approx 4$ km on time scales longer than 2–3 LF forcing periods [WTL].

In all three primary scenarios presented in this paper (LF, HF, LFHF), the maximum (in y) P_{int} is found at $y \approx 4$ km, where most of the increase in the phytoplankton concentration P occurs at the SPM in all three cases (Figure 7). Here at $y \approx 4$ km, P_{int} increases by 200% after 32 days of LF or LFHF forcing and 50% after 32 days of HF forcing (relative to the initial condition or outside the front; see Figure 5d). Thus, a question arises: is the wind-driven advection or wind-driven vertical mixing responsible for these significant increases in P_{int} at $y \approx 4$ km?

In order to demonstrate that wind-driven advection (rather than wind-driven vertical mixing) is the dominant driver of the elevated P in the SPM at $y \approx 4$ km under all three wind scenarios, Figures 9 and 10 highlight several comparisons between the three primary scenarios and the three analog scenarios with the same wind forcing but without variable mixing (i.e., with constant mixing CM) of biogeochemical tracers (see Table 1 and section 2.1 for a description of the CM scenarios). In particular, Figure 9b shows that P_{int} at $y \approx 4$ km and $t = 30$ days is increased by less than 20% in the three primary KPP mixing scenarios relative to the three CM scenarios. Hence, at $y \approx 4$ km, the percent difference in P_{int} between a given KPP scenario and its analog CM scenario ($\leq 20\%$) is small relative to the percent difference between P_{int} in a given forcing scenario and the initial condition (50–200%; see Figure 5d).

In addition, the biogeochemical response to surface mixing, which results in an increase in phytoplankton at low concentrations in the SXL, differs qualitatively from the biogeochemical response to a steady

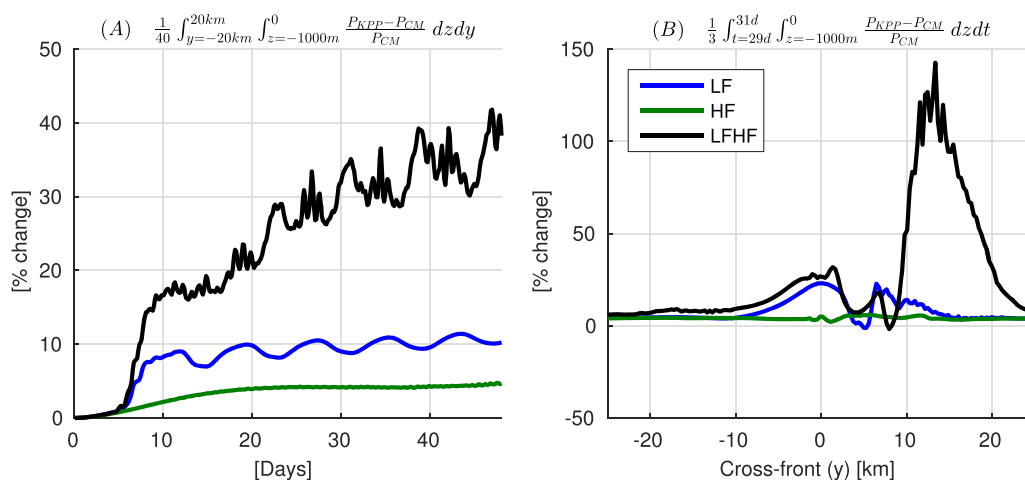


Figure 9. Average (a: from $y = -20$ to 20 km) and (b: from $t = 29$ to 31 days) percent change in full-depth-integrated phytoplankton $P_{int} = \int_{z=-1000m}^0 P dz$ due to variable KPP-mixing of biogeochemical tracers. The percent changes are relative to the analog CM simulations that are physically identical to the KPP simulations except for the vertical diffusivity of biogeochemical tracers, which is set to a constant background diffusivity of $K_z = 2 \times 10^{-5} \text{ m}^2/\text{s}$ in the CM scenarios (see section 2.1).

upwelling by advection, which results in an accumulation of phytoplankton at high concentration in the SPM [WTL]. Hence, we plot histograms of phytoplankton concentrations in Figure 10. These histograms clarify whether the increase in phytoplankton biomass occurs at low or high phytoplankton concentrations and therefore help in identifying the relative significance of surface mixing and vertical advection in driving increases in P_{int} . In particular, the accumulation of biomass at higher phytoplankton concentrations in the SPM (i.e., $P > 0.6 \text{ mmol N/m}^2$), which occurs in both the primary KPP-mixing and analog CM scenarios, is qualitatively inconsistent with the phytoplankton response to episodic surface mixing, which tends to induce phytoplankton biomass accumulation at relatively low phytoplankton concentrations in the SXL and reduce phytoplankton concentrations at the SPM (Figure 1).

Finally, nutrient entrainment into the SXL is negligible after the first LF forcing period (i.e., after 8 days) near $y = 4$ km, because SXLs are too shallow and too far from the nutricline there (Figure 11). Hence, the variable mixing does not strongly influence the nutricline and the SPM, since the vertical diffusivity is generally small below the SXL, even with KPP activated. Together, these results suggest that advection—not vertical mixing—induced by the oscillatory wind is the primary driver of the increased P in the SPM at $y \approx 4$ km.

3.3.2. Enhanced Phytoplankton in the Surface Mixing Layer

Figure 9b reveals a striking difference between the LFHF scenarios with and without wind-driven variable vertical mixing of biogeochemical tracers. In particular, from $y \approx 10$ to 20 km, where SXLs are deepest and closest to the nutricline (Figure 11), nutrient is episodically entrained into the SXL (Figures 5e and 5f), P is persistently elevated in the SXL (Figure 8d), and the variable wind-driven vertical mixing induces a 100% increase in P_{int} relative to the initial condition (Figure 5d).

Averaged across the front from $y = -20$ to 20 km, the wind-driven variable KPP mixing is responsible for a 40% increase in P_{int} over 48 days of LFHF wind relative to the CM scenario (Figure 9a), which is comparable in magnitude to the overall 50% increase in cross-front averaged P_{int} due to both advection and mixing in the KPP scenario relative to the initial condition (Figure 5c). In addition, after three LF periods (24 days) of LFHF wind, the distribution of depth-integrated phytoplankton biomass in concentration space at $y = 12$ km (Figure 10c) shows a significant increase in biomass at low concentrations (i.e., $P < 0.4 \text{ mmol N/m}^3$) and a somewhat smaller reduction in biomass at higher concentrations (i.e., $P > 0.4 \text{ mmol N/m}^3$) relative to the initial condition, which is consistent with the effects of intermittent surface mixing (Figure 1). In contrast, the analog LFHF CM scenario shows little change in the distribution of phytoplankton mass fraction at $y = 12$ km (Figure 10d) or averaged across the front (Figure 10b). In fact, the distribution of phytoplankton mass fraction in the LFHF CM scenario is more similar to the distribution in the LF scenario (Figure 10), because the wind-driven advection is the dominant driver of the biogeochemical changes in both the LFHF CM and LF scenarios.

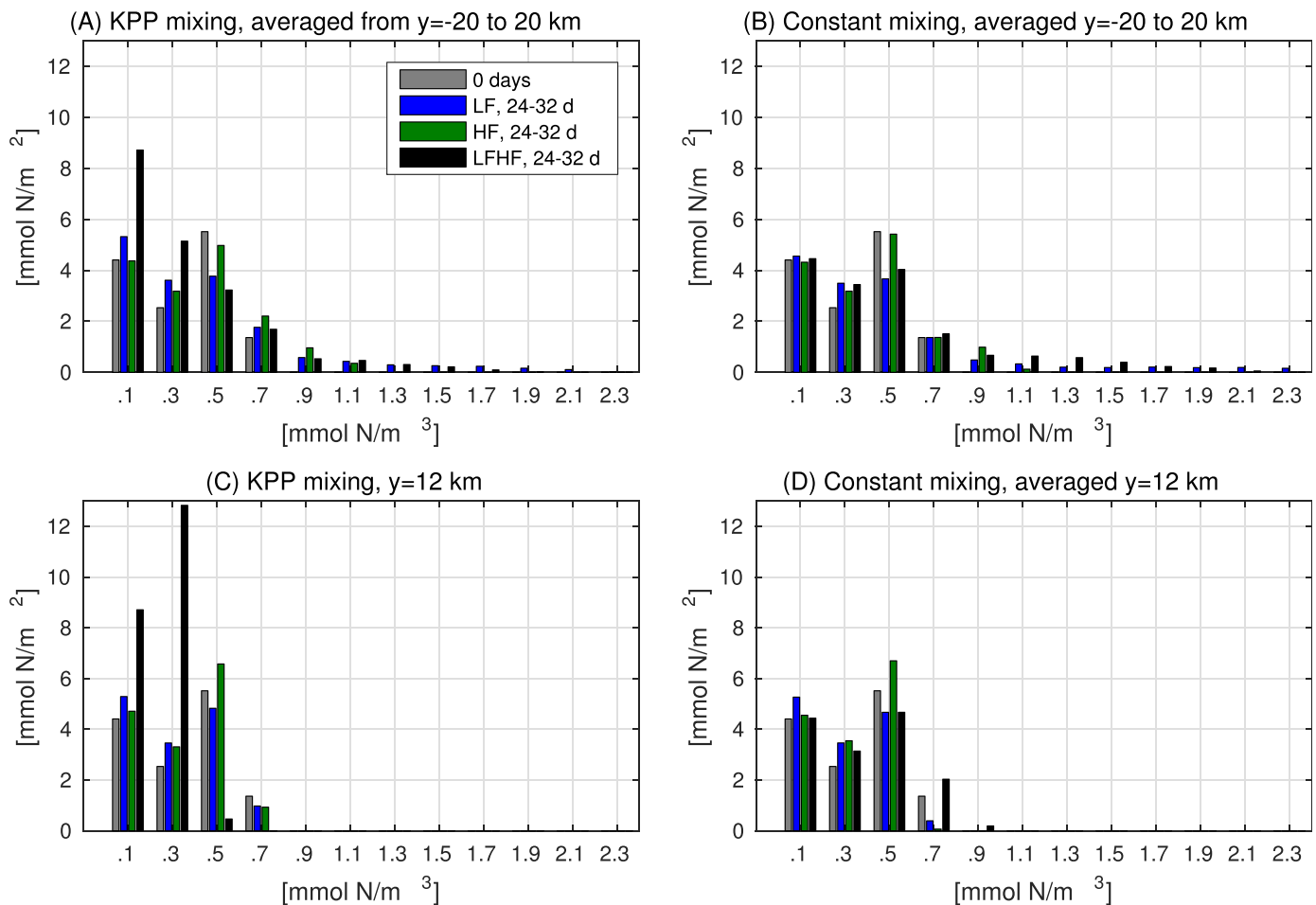


Figure 10. Histograms of the full-depth-integrated phytoplankton mass fraction at each concentration under LF (blue bars), HF (green bars), and LFHF (black bars) wind stress: (a) averaged from $y = -20$ to 20 km with wind-driven KPP mixing of biogeochemical tracers, (b) averaged from $y = -20$ to 20 km without variable wind-driven KPP mixing of biogeochemical tracers (i.e., in the analog CM scenarios; see section 2.1), (c) at $y = 12$ km with wind-driven KPP mixing of biogeochemical tracers, and (d) at $y = 12$ km without variable wind-driven KPP mixing of biogeochemical tracers (i.e., in the CM scenarios). All bars represent averages over the fourth LF forcing period, from 24 to 32 days, which coincides with the snapshots shown in Figures 5 and 7. The gray bars denote the initial state, which is the same in all four plots. Here the i th bar of each histogram is calculated from $\int_{z=-1000}^0 P(z) \mathcal{I}(P) dz$ where the indicator function $\mathcal{I}(P) = 1$ if $P_i \leq P < P_{i+1}$ and the $P_i = [0, 0.2, 0.4, \dots, 2.4]$. Hence, the sum of all bars in each histogram (of a given color/in a given scenario) represents P_{int} in that scenario.

Hence, the significant biogeochemical differences between the LFHF scenario and LF scenario are largely due to the vertical mixing and nutrient entrainment on the less dense side of the front induced by the addition of the small-amplitude HF wind. In particular, differences between the LF and LFHF scenarios in primary production and zooplankton grazing rates and thus phytoplankton accumulation rates (Figures 5c, 5d, 5g, and 5j) are largely due to the wind mixing and nutrient entrainment under LFHF wind on the less dense side of the front. The intermittent deep mixing events induce intermittent nutrient entrainment pulses under LFHF wind (Figures 5e and 5f), which induce simultaneous transient increases (by 20%) in the cross-front averaged (from $y = -20$ to 20 km) and full-depth-integrated primary production UP [defined in (5)] (Figure 5g). Moreover, the full-depth-integrated primary production in the LFHF scenario doubles relative to the LF scenario at the cross-front location where nutrients are entrained (e.g., $y \approx 12$ km in Figure 5h). Zooplankton grazing responds more slowly in time than primary production to the physical perturbations, but the cross-front averaged grazing rate decreases transiently by about 5% simultaneously with the spikes in primary production induced by LFHF wind (Figure 5i), and the full-depth-integrated grazing rate remains lower at $y \approx 12$ km than outside the front, even though primary production is elevated there (Figure 5j).

On the other hand, the small-amplitude HF wind has little biogeochemical effect without the LF wind, because it is insufficient on its own to drive significant nutrient entrainment and mixing. Plots of the SXL

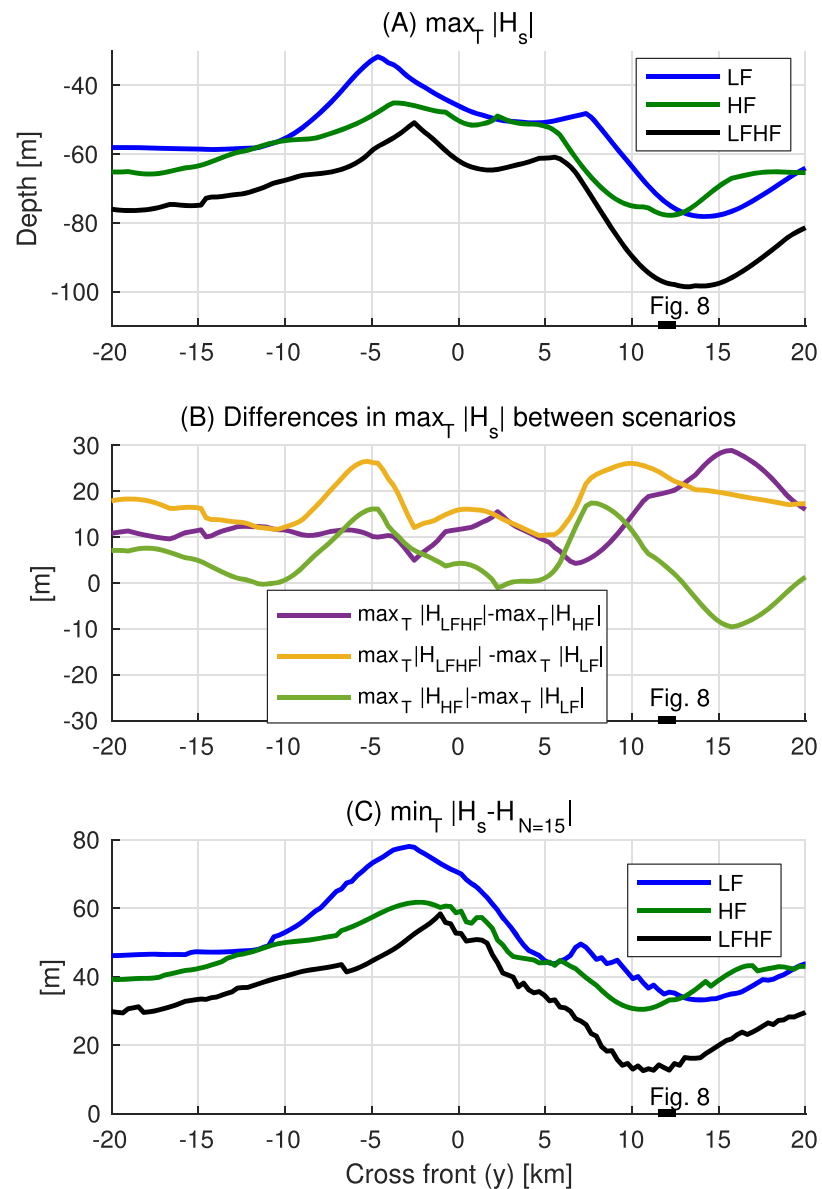


Figure 11. Cross-front variations in: (a) maximum mixing layer depth in each scenario, (b) differences in maximum mixing layer depths between the scenarios, and (c) minimum distance in each scenario between the base of the mixing layer, H_s , and the $N = 15$ isopleth depth, $H_{N=15}$, which is a proxy for the distance between the mixing layer base and the nutricline. The maxima and minima are calculated during the fourth LF forcing period, over the time interval T , which ranges from 24 to 32 days and coincides with the time interval chosen in Figures 5, 7, and 10.

depth and the distance between the SXL base and the nutricline $|H_s - H_{N=15}|$ highlight the synergistic effect that the LF and HF winds have on the SXL and hence nutrient entrainment on the less dense side of the front. In particular, both the high-amplitude LF wind and the low-amplitude HF wind induce significant mixing and deepen the SXL across the front. Yet, in both cases, the SXLs are deepest and closest to the nutricline on the less dense side of the front (Figure 11). Hence, the greatest increases in the magnitude of the SXL depth between the LF or HF scenarios and LFHF scenario occur on the less dense side of the front, between $y \approx 10$ and 15 km (Figure 11b), where SXLs are already deeper and closer to the nutricline than the more dense side of the front or outside the front. Hence, LF and HF winds act synergistically to maintain a cross-front asymmetry in SXL depth with deeper mixing layers and more nutrient entrainment into the SXL on the less dense side of the front. Therefore, LF and HF along-front winds have a synergistic effect on phytoplankton in particular, and biogeochemistry in general, at fronts in nutrient-limited open-ocean conditions.

3.4. Sensitivity to Wind Direction and Frequency

At this stage, some questions may remain as to how the biogeochemical impacts induced by combined LFHF wind depend on the direction and frequency content of the wind. WTL explore the sensitivity of the biogeochemical response to different LF winds and find that the LF dynamics are qualitatively similar for different low frequencies (4–16 day periods) and amplitudes (.06–.24 N/m^2). Here we consider the following sets of questions:

1. How sensitively does the biogeochemical response to LFHF wind depend on the frequency content of the HF part of the wind? Would any additional HF oscillatory wind drive nutrient entrainment where and when the modifications to the stratification by the LF Ekman buoyancy flux [*EBF* defined in (1)] make the front more susceptible to entrainment (that is, on the less dense side of the front when the time-integrated *EBF* [defined in (2)] is maximum)? Are the near-inertial high frequencies more effective (at a given fixed amplitude) than other high frequencies at driving entrainment and enhancing phytoplankton biomass?
2. How sensitively does the biogeochemical response to combined low and high-frequency wind depend on the modification to the underlying stratification driven by the LF *EBF*? For example, how does the biogeochemical response differ if the oscillatory winds are oriented perpendicular to the front, whence $EBF = 0 \text{ m}^2/\text{s}^3$? That is, how might the biogeochemical effects of an oscillating along-front wind stress differ from those due to oscillating turbulent mixing in the surface layer (energized by any process, e.g., surface gravity waves, winds, surface heat loss, etc.), which could also drive vertical circulations and nutrient entrainment in fronts in the absence of an explicit along-front stress [e.g., *Garrett and Loder, 1981; Nagai et al., 2008*]?

The first question is addressed using results from a series of sensitivity simulations labeled “S” in Table 1 and plotted in Figure 12, which are identical to the simulations with wind-driven vertical mixing that are discussed in previous sections except for the magnitude, frequency, and direction of the winds. These S simulations are forced by one LF harmonic $\tau_x^L = .12 \cos(.09ft)$ (an 8 day period) and one HF harmonic

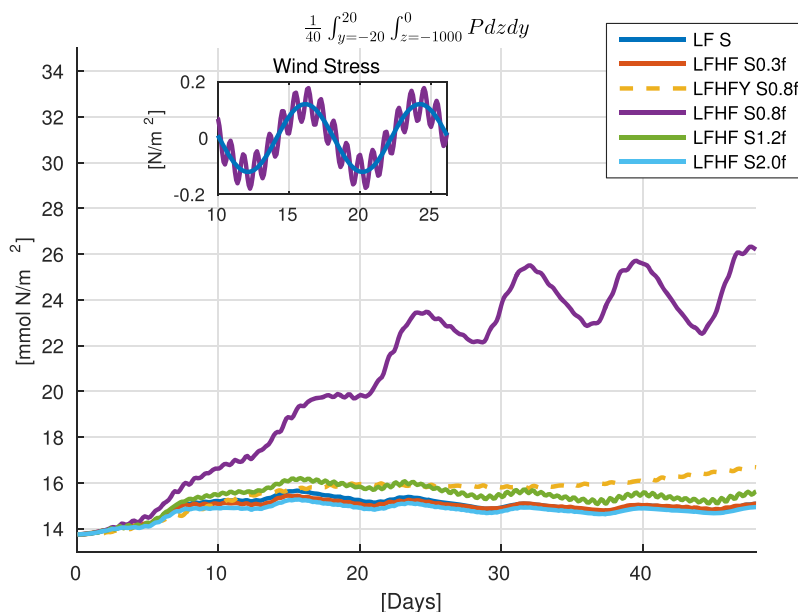


Figure 12. Full-depth-integrated phytoplankton biomass P_{int} as a function of time and averaged across the front (from $y = -20$ to 20 km) in six sensitivity experiments forced by different low-frequency and high-frequency wind stress: LF S is forced by only a low-frequency along-front wind stress oriented parallel to the front that has a lower amplitude (.12 N/m^2) than the default LF experiment (.18 N/m^2) but the same frequency (see Table 1, the LF S wind stress is shown in blue in the inset plot). The LFHF S scenarios are forced by both low-frequency (.12 N/m^2) and high-frequency (.06 N/m^2) along-front winds, where the high frequency is composed of only a single frequency, which ranges from $0.3f$ to $2.0f$ as indicated in the legend. The LFHF Y S scenario (yellow dashes) differs in that it is forced by low-frequency and high-frequency wind stresses oriented perpendicular to (i.e., across) the front. Except when the high frequency resonates on the less dense side of the front, where $\omega^H = 0.8f \approx f_e$, all of the scenarios essentially overlap because the high-frequency wind has essentially no impact on the biogeochemistry unless it triggers the resonant generation of near-inertial oscillations, consistent with the hypotheses in section 1.1.

$\tau_x^H = 0.06 \cos(\omega^H t)$ with high frequencies ranging from $\omega^H = 0.3f$ to $2.0f$ (2.4–0.4 day periods). The results demonstrate that the phytoplankton response to combined LFHF wind depends strongly on the particular high frequency. As hypothesized in section 1.1, frequencies just below the Coriolis frequency, which resonate on the less dense side of the front where $f_e < f$ [see (3)], induce the strongest biogeochemical response. In particular, the cross-front averaged ($y = -20$ to 20 km) P_{int} increases by about 90% relative to the initial condition (180% from $y = 0$ to 20 km, not shown) over 48 days of wind forcing with $\omega^H = 0.8f$ just below the inertial frequency. In contrast, the cross-front averaged ($y = -20$ to 20 km) P_{int} increases by at most 25% relative to the initial condition when the HF is either well below the inertial frequency ($\omega^H = 0.3f$), just above the inertial frequency ($\omega^H = 1.2f$), or well above the inertial frequency ($\omega^H = 2.0f$). The increase in P when $\omega^H = 0.8f$ is due to episodic nutrient entrainment fluxes that are maximum at about $y \approx 10$ km and occur when time-integrated *EBF* and *SXL* depth are approaching a local maximum on the less-dense side of the front (not shown), as in the primary LFHF scenario discussed in previous sections (see Figure 6). Hence, although any high frequency stress can eventually drive nutrient entrainment at a sufficiently high amplitude, near-inertial frequencies just below the Coriolis frequency are more effective (for a given wind stress amplitude) at inducing nutrient entrainment in combination with the LF along-front stress.

With regards to the second question, this paper hypothesizes that the synergistic biogeochemical response to LFHF wind depends strongly on the time-integrated *EBF* [defined in (2)], hence the direction of the wind stress relative to the front. To make this directional dependence more explicit, we contrast the sensitivity simulation that induces the largest biogeochemical response (the purple line labeled LFHF S 0.8f in Figure 12, see Table 1) with another sensitivity simulation that is forced by a wind stress with exactly the same amplitudes and frequency components but a perpendicular cross-front orientation (the yellow dashed line labeled LFHF Y S 0.8f in Figure 12, see Table 1).

The results of this comparison underscore the results of previous sections: the deepest *SXLs* on the less dense side of the front (not shown) and hence the phytoplankton response to combined LFHF wind (Figure 12) depends strongly on the direction of the wind. As discussed in previous sections, along-front winds induce significant changes in the frontal stratification and *SXL* depth due to the Ekman buoyancy flux, hence deeper mixing layers and a stronger biogeochemical response. In particular, the cross-front averaged ($y = -20$ to 20 km) P_{int} increases by about 90% (relative to the initial condition) after 48 days of along-front LFHF wind, compared to 20% after 48 days of across-front LFHF wind.

4. Conclusions and Discussion

4.1. Conclusions

By analyzing several example model scenarios, this paper advances the hypothesis that intermittent and anomalously deep wind-driven surface mixing layers contribute to sustaining primary production and spatially integrated phytoplankton biomass in nutrient-limited open-ocean conditions. Moreover, a previously unidentified physical mechanism is put forward wherein oscillatory along-front winds, with frequencies characteristic of atmospheric variability on time scales ranging from about a week to about a day, induce anomalously deep mixing layers on the less dense side of geostrophic fronts, which are ubiquitous features of the upper ocean. The conclusions are based on theory and idealized simulations.

The results demonstrate how intermittent and cyclic deep surface mixing can create a cyclostationary equilibrium with an intermittent and less-concentrated subsurface phytoplankton maximum and more phytoplankton distributed over shallower depths than in the absence of intermittent surface mixing (Figures 1 and 2). Moreover, the time-averaged and full-depth-integrated phytoplankton biomass, growth rates, and grazing rates increase very nonlinearly when the mixing layer depth penetrates the nutricline; that is, slight increases in the mixing layer depth lead to large increases in phytoplankton.

Although many different physical mechanisms may lead to spatial and temporal variability in the surface mixing layer depth, oscillatory winds with time scales ranging from about a week (low-frequency) to about a day (high-frequency) induce anomalously deep mixing layers at geostrophic fronts. In particular, the deepest mixing layers at geostrophic fronts depend on:

1. wind-driven changes in the upper-ocean stratification by the low-frequency Ekman buoyancy flux [defined in (1)], that is the cross-front transport of buoyancy by the Ekman flow, and

2. the frequency-dependent deepening of surface mixing layer due to the resonant oceanic response to winds with variance near the effective Coriolis frequency f_e [defined in (3)].

With regard to the wind-driven changes in stratification at fronts, over much of the midlatitude oceans, synoptic and planetary atmospheric variability with time scales ranging from several days to a few weeks represents a large fraction of the total wind stress variance [e.g., Alford, 2001; Gille, 2005]. The qualitative description of the simulation forced by low-frequency and high-frequency wind (section 3.1 and Figure 6) highlights the substantial impact that oscillatory low-frequency Ekman buoyancy flux has on the stratification and surface mixing layer depths across the front. Making an analogy between oscillatory Ekman buoyancy fluxes and oscillatory surface heat fluxes clarifies why the deepest mixing layers, most nutrient entrainment, and fastest primary production and phytoplankton accumulation rates all lag the strongest wind stresses and instead coincide with maxima in the surface density, the full-depth-integrated density, and the time-integrated Ekman buoyancy flux [defined in (2)]. The oscillatory Ekman buoyancy flux drives oscillations in the upper-ocean heat content with a magnitude of 85 MJ/m² every 4 days (see Figure 5b). For perspective, an 85 MJ/m² loss of upper-ocean heat could also be induced by a sustained surface heat flux with a magnitude of 250 W/m² integrated over 4 days.

With regard to the frequency-dependent deepening of the surface mixing layer at fronts, although the near-inertial high-frequencies do not represent a large fraction of the total wind stress variance, the near-inertial band contains a large fraction of the upper-ocean kinetic energy due to the resonant amplification of inertial currents [e.g., Pollard and Millard, 1970; Elipot and Lumpkin, 2008]. Comparing the simulation forced by both low-frequency and high-frequency winds with simulations forced by only low-frequency winds (section 3.2 and Figures 5, 7, and 8) underscores the significant impact that the low-amplitude high-frequency near-inertial winds have on the deepening of the surface mixing layer across the front (Figure 11), particularly on the less dense side of the front. Moreover, sensitivity simulations emphasize that the biogeochemical impacts associated with the deepening of the surface mixing layer depend on the particular high-frequency: phytoplankton accumulation at the front is much greater for high-frequencies just below the local Coriolis frequency, which resonate where the effective Coriolis frequency $f_e < f$ (3) and therefore do more work on the less dense side of the front; other high frequencies that are far from f_e on the less dense side of the front do not resonate and induce a negligible biogeochemical response (Figure 12).

Although spatially integrated phytoplankton can only increase due to inherently biogeochemical rather than physical processes, that is imbalances between growth and loss rates, the physical transport of biogeochemical constituents by advection and vertical mixing drives—albeit indirect—all of the biogeochemical changes. Due to the significant spatial and temporal variability in mixing and advection across a front forced by oscillatory wind, the instantaneous full-depth-integrated primary production varies by as much as a factor of 3 across the front and the cross-front averaged primary production varies by as much as 75% in time (Figures 5g and 5h). Zooplankton grazing rates exhibit similar cross-front variations, but smaller temporal variations than primary production due to the longer zooplankton response time scale (relative to phytoplankton, see Figures 5i and 5j).

The different fingerprints of wind-driven turbulent mixing and advection on biogeochemistry are identified in the distributions of phytoplankton biomass in depth and concentration space (Figures 1, 7, and 10): mixing tends to increase phytoplankton biomass at low concentrations in a diffuse surface mixing layer, whereas upward advection tends to increase phytoplankton biomass at high concentrations at the subsurface phytoplankton maximum. Vertical advection of nutrient induced by oscillatory wind has a significant impact on full-depth-integrated phytoplankton at the front, particularly when surface mixing layers do not reach the nutricline (section 3.3.1). However, when the deepest surface mixing layers intermittently reach the nutricline under low-frequency and high-frequency wind, phytoplankton accumulate so rapidly that the total increase in full-depth-integrated phytoplankton averaged across the front is mostly due to mixing and nutrient entrainment (section 3.3.2).

4.2. Discussion

As in other process studies of physics and biogeochemistry, many details in these results may depend on a range of physical and biogeochemical parameters that vary in both models and the real ocean, from the magnitude of the stratification and the potential vorticity in the pycnocline to the gradient and depth of

the nutricline, as well as the ratio of the mixing layer to frontal depth. Some but not all of these sensitivities are discussed in WTL and Franks and Walstad [1997], and further investigation of the remaining sensitivities will have to wait for future work. Moreover, although there is a qualitative correspondence between the theoretical notions (section 1.1) and the numerical results (section 3), this should not be taken to imply that the theories, which omit many different physical processes active in the simulations, fully explain the simulations. Rather, the results suggest that the theoretical ideas in section 1.1 provide a useful starting point for thinking about the dynamics of the simulations, and possibly the real ocean.

In addition, several physical processes that occur in the real ocean are omitted or crudely represented in these numerical experiments. A particular concern is three-dimensional meandering, frontogenesis and mixed layer restratification processes, which have been discussed elsewhere to some degree [e.g., Lévy *et al.*, 2009; Mahadevan *et al.*, 2012; Brannigan, 2016]. Finally, the results of the numerical simulations are obtained with an ocean model where surface mixing layer turbulence and entrainment is parameterized. Hence, the results may depend on this parameterization (KPP), which is widely used in both physical and coupled physical-biogeochemical ocean models, including in submesoscale resolving simulations. Although the qualitative consistency between these results and those of Lévy *et al.* [2009] (who used a different boundary-layer turbulence model) are encouraging, these results should be viewed as representative of the physics in this model and parameterization, until efforts are made to validate these results with observations and large eddy simulations. A particular concern is whether or not KPP can accurately represent surface mixing in the stratified transition layer at the top of the pycnocline, which may be crucial for maintaining the nutrient supply to the euphotic zone in nutrient-limited conditions [e.g., Forryan *et al.*, 2015; Nicholson *et al.*, 2016].

Despite the limitations of this particular study, it seems likely that the synergistic oceanic response to low-frequency and high-frequency wind could have a significant impact on the stratification (i.e., upper-ocean heat content), nutrient entrainment and biogeochemistry at fronts in the real ocean as well as in mesoscale or submesoscale resolving simulations with air-sea fluxes that are characterized by realistic or idealized frequency spectra with significant variance at both low and high frequencies. Hence, coupled ocean physical and biogeochemical models that under represent or omit the high-frequency part of the wind forcing and/or mesoscale and submesoscale variability in the upper-ocean physics may systematically misrepresent the rates of primary production and the total phytoplankton biomass; the very preliminary experiments presented here suggest that such errors might be on the order of 10–100% and that these processes will tend to increase total primary production and phytoplankton biomass in nutrient-limited oceans.

Acknowledgments

The simulation output can be obtained by emailing the lead author (dan.whitt@gmail.com). D.B.W. was supported by an NSF postdoctoral research fellowship, award 1421125. J.R.T. was supported by NERC award NE/J010472/1. The simulations and analysis were performed in part using computing resources provided by the Department of Applied Maths and Theoretical Physics at the University of Cambridge. The constructive input from two reviewers significantly improved the presentation.

References

- Alford, M. (2001), Internal swell generation: The spatial distribution of energy flux from the wind to mixed layer near-inertial motions, *J. Phys. Oceanogr.*, *31*(8), 2359–2368.
- Allen, J. T., et al. (2005), Diatom carbon export enhanced by silicate upwelling in the northeast Atlantic, *Nature*, *437*(7059), 728–732.
- Beckmann, A., and I. Hense (2007), Beneath the surface: Characteristics of oceanic ecosystems under weak mixing conditions—A theoretical investigation, *Prog. Oceanogr.*, *75*(4), 771–796.
- Belkin, I. M., P. C. Cornillon, and K. Sherman (2009), Fronts in large marine ecosystems, *Prog. Oceanogr.*, *81*(1), 223–236.
- Brannigan, L. (2016), Intense submesoscale upwelling in anticyclonic eddies, *Geophys. Res. Lett.*, *43*, 3360–3369, doi:10.1002/2016GL067926.
- Carranza, M. M., and S. T. Gille (2015), Southern ocean wind-driven entrainment enhances satellite chlorophyll-a through the summer, *J. Geophys. Res. Oceans*, *120*, 304–323, doi:10.1002/2014JC010203.
- Claustre, H., P. Kerhervé, J. C. Marty, L. Prieur, C. Videau, and J.-H. Hecq (1994), Phytoplankton dynamics associated with a geostrophic front: Ecological and biogeochemical implications, *J. Mar. Res.*, *52*(4), 711–742.
- Crawford, G., and W. Large (1996), A numerical investigation of resonant inertial response of the ocean to wind forcing, *J. Phys. Oceanogr.*, *26*, 873–891.
- Cullen, J. J. (2015), Subsurface chlorophyll maximum layers: Enduring enigma or mystery solved?, *Annu. Rev. Mar. Sci.*, *7*, 207–239.
- Cushman-Roisin, B. (1987), Subduction, in *Dynamics of the Ocean Mixed Layer*, edited by P. Muller and D. Henderson, pp. 181–196, Spec. Publ., Hawaii Inst. for Geophys., Honolulu.
- Danioux, E., J. Vanneste, and O. Bühler (2015), On the concentration of near-inertial waves in anticyclones, *J. Fluid Mech.*, *773*, R2.
- D'Asaro, E. (1985a), The energy flux from the wind to near-inertial motions in the surface mixed layer, *J. Phys. Oceanogr.*, *15*, 1043–1059.
- D'Asaro, E. A. (1985b), Upper ocean temperature structure, inertial currents, and Richardson numbers observed during strong meteorological forcing, *J. Phys. Oceanogr.*, *15*(7), 943–962.
- D'Asaro, E. A., C. C. Eriksen, M. D. Levine, P. Niiler, C. Paulson, and P. van Meurs (1995), Upper-ocean inertial currents forced by a strong storm. Part I: Data and comparisons with linear theory, *J. Phys. Oceanogr.*, *25*, 2909–2936.
- Davis, R. E., M. D. Ohman, D. L. Rudnick, and J. T. Sherman (2008), Glider surveillance of physics and biology in the southern California current system, *Limnol. Oceanogr.*, *53*(5part2), 2151–2168.
- De Zoete, R. A. (1980), On the effects of horizontal variability of wind stress on the dynamics of the ocean mixed layer, *J. Phys. Oceanogr.*, *10*(9), 1439–1454.

- Doney, S., D. M. Glover, and R. Najjar (1996), A new coupled, one-dimensional biological-physical model for the upper ocean: Applications to the JGOFS Bermuda Atlantic time-series study (BATS) site, *Deep Sea Res., Part II*, 43(2–3), 591–624.
- Edwards, A. M., and J. Brindley (1999), Zooplankton mortality and the dynamical behaviour of plankton population models, *Bull. Math. Biol.*, 61(2), 303–339.
- Edwards, A. M., and A. Yool (2000), The role of higher predation in plankton population models, *J. Plankton Res.*, 22(6), 1085–1112.
- Elipot, S., and R. Lumpkin (2008), Spectral description of oceanic near-surface variability, *Geophys. Res. Lett.*, 35, L05606, doi:10.1029/2007GL032874.
- Elipot, S., R. Lumpkin, and G. Prieto (2010), Modification of inertial oscillations by the mesoscale eddy field, *J. Geophys. Res.*, 115, C09010, doi:10.1029/2009JC005679.
- Fedorov, K. N. (1986), *The Physical Nature and Structure of Ocean Fronts*, Springer-Verlag, New York, N. Y.
- Fernández, E., and R. D. Pingree (1996), Coupling between physical and biological fields in the north Atlantic subtropical front southeast of the Azores, *Deep Sea Res., Part I*, 43(9), 1369–1393.
- Forryan, A., A. C. Naveira Garabato, K. L. Polzin, and S. Waterman (2015), Rapid injection of near-inertial shear into the stratified upper ocean at an Antarctic circumpolar current front, *Geophys. Res. Lett.*, 42, 3431–3441, doi:10.1002/2015GL063494.
- Franks, P., and L. Walstad (1997), Phytoplankton patches at fronts: A model of formation and response to wind events, *J. Mar. Res.*, 55(1), 1–29.
- Franks, P., J. Wroblewski, and G. Flierl (1986), Behavior of a simple plankton model with food-level acclimation by herbivores, *Mar. Biol.*, 91(1), 121–129.
- Garrett, C., and J. Loder (1981), Dynamical aspects of shallow sea fronts, *Philos. Trans. R. Soc. London A*, 302(1472), 563–581.
- Gill, A. E. (1982), *Atmosphere-Ocean Dynamics*, Academic, London.
- Gille, S. T. (2005), Statistical characterization of zonal and meridional ocean wind stress, *J. Atmos. Oceanic Technol.*, 22(9), 1353–1372.
- Granata, T., J. Wiggert, and T. Dickey (1995), Trapped, near-inertial waves and enhanced chlorophyll distributions, *J. Geophys. Res.*, 100(C10), 20,793–20,804.
- Grisouard, N., and L. N. Thomas (2016), Energy exchanges between density fronts and near-inertial waves reflecting off the ocean surface, *J. Phys. Oceanogr.*, 46(2), 501–516.
- Gruber, N., and J. Sarmiento (2002), Large-scale biogeochemical-physical interactions in elemental cycles, *The Sea*, 12, 337–399.
- Gruber, N., Z. Lachkar, H. Frenzel, P. Marchesiello, M. Münnich, J. C. McWilliams, T. Nagai, and G.-K. Plattner (2011), Eddy-induced reduction of biological production in eastern boundary upwelling systems, *Nat. Geosci.*, 4(11), 787–792.
- Guidi, L., et al. (2012), Does eddy-eddy interaction control surface phytoplankton distribution and carbon export in the north Pacific subtropical gyre?, *J. Geophys. Res.*, 117, G02024, doi:10.1029/2012JG001984.
- Hitchcock, G. L., A. J. Mariano, and T. Rossby (1993), Mesoscale pigment fields in the Gulf Stream: Observations in a meander crest and trough, *J. Geophys. Res.*, 98(C5), 8425–8445.
- Hoskins, B. (1974), The role of potential vorticity in symmetric stability and instability, *Q. J. R. Meteorol. Soc.*, 100, 480–482.
- Inoue, R., M. C. Gregg, and R. R. Harcourt (2010), Mixing rates across the Gulf Stream, Part 1: On the formation of eighteen degree water, *J. Mar. Res.*, 68, 643–671.
- Jochum, M., B. P. Briegleb, G. Danabasoglu, W. G. Large, N. J. Norton, S. R. Jayne, M. H. Alford, and F. O. Bryan (2013), The impact of oceanic near-inertial waves on climate, *J. Clim.*, 26(9), 2833–2844.
- Joyce, T., J. Toole, P. Klein, and L. Thomas (2013), A near-inertial mode observed within a Gulf Stream warm-core ring, *J. Geophys. Res. Oceans*, 118, 1797–1806, doi:10.1002/jgrc.20141.
- Klein, P., and B. Coste (1984), Effects of wind-stress variability on nutrient transport into the mixed layer, *Deep Sea Res., Part A*, 31(1), 21–37.
- Klein, P., and G. Lapeyre (2009), The oceanic vertical pump induced by mesoscale and submesoscale turbulence, *Annu. Rev. Mar. Sci.*, 1, 351–375.
- Klein, P., G. Lapeyre, and W. Large (2004), Wind ringing of the ocean in presence of mesoscale eddies, *Geophys. Res. Lett.*, 31, L15306, doi:10.1029/2004GL020274.
- Kouketsu, S., H. Tomita, E. Oka, S. Hosoda, T. Kobayashi, and K. Sato (2012), The role of meso-scale eddies in mixed layer deepening and mode water formation in the western north Pacific, *J. Oceanogr.*, 68(1), 63–77.
- Krause, J. W., M. A. Brzezinski, R. Goericke, M. R. Landry, M. D. Ohman, M. R. Stukel, and A. G. Taylor (2015), Variability in diatom contributions to biomass, organic matter production and export across a frontal gradient in the California current ecosystem, *J. Geophys. Res. Oceans*, 120, 1032–1047, doi:10.1002/2014JC010472.
- Kunze, E. (1985), Near-inertial wave propagation in geostrophic shear, *J. Phys. Oceanogr.*, 15, 544–565.
- Kunze, E., R. W. Schmidt, and J. M. Toole (1995), The energy balance in a warm core ring's near-inertial critical layer, *J. Phys. Oceanogr.*, 25, 942–957.
- Large, W., J. McWilliams, and P. Niiler (1986), Upper ocean thermal response to strong autumnal forcing of the northeast Pacific, *J. Phys. Oceanogr.*, 16(9), 1524–1550.
- Large, W. G., J. C. McWilliams, and S. C. Doney (1994), Oceanic vertical mixing: A review and a model with a nonlocal boundary layer parameterization, *Rev. Geophys.*, 32, 363–403.
- Lee, C. M., L. N. Thomas, and Y. Yoshikawa (2006), Intermediate water formation at the Japan East Sea subpolar front, *Oceanography*, 19, 110–121.
- Lévy, M., P. Klein, and M. Ben Jelloul (2009), New production stimulated by high-frequency winds in a turbulent mesoscale eddy field, *Geophys. Res. Lett.*, 36, L16603, doi:10.1029/2009GL039490.
- Lévy, M., R. Ferrari, P. J. Franks, A. P. Martin, and P. Rivière (2012a), Bringing physics to life at the submesoscale, *Geophys. Res. Lett.*, 39, L14602, doi:10.1029/2012GL052756.
- Lévy, M., D. Iovino, L. Resplandy, P. Klein, G. Madec, A.-M. Tréguier, S. Masson, and K. Takahashi (2012b), Large-scale impacts of submesoscale dynamics on phytoplankton: Local and remote effects, *Ocean Model.*, 43, 77–93.
- Li, Q. P., P. J. Franks, M. D. Ohman, and M. R. Landry (2012), Enhanced nitrate fluxes and biological processes at a frontal zone in the southern California current system, *J. Plankton Res.*, 790–801.
- Mahadevan, A. (2016), The impact of submesoscale physics on primary productivity of plankton, *Annu. Rev. Mar. Sci.*, 8, 161–184.
- Mahadevan, A., L. N. Thomas, and A. Tandon (2008), Comment on “Eddy/Wind interactions stimulate extraordinary mid-ocean plankton blooms”, *Science*, 320(5875), 448–448.
- Mahadevan, A., A. Tandon, and R. Ferrari (2010), Rapid changes in mixed layer stratification driven by submesoscale instabilities and winds, *J. Geophys. Res.*, 115, C03017, doi:10.1029/2008JC005203.

- Mahadevan, A., E. D'Asaro, C. Lee, and M. J. Perry (2012), Eddy-driven stratification initiates north Atlantic spring phytoplankton blooms, *Science*, 337(6090), 54–58.
- Marra, J., R. Bidigare, and T. Dickey (1990), Nutrients and mixing, chlorophyll and phytoplankton growth, *Deep Sea Res., Part A*, 37(1), 127–143.
- Martin, A. (2003), Phytoplankton patchiness: The role of lateral stirring and mixing, *Prog. Oceanogr.*, 57(2), 125–174.
- Martin, A. P., and K. J. Richards (2001), Mechanisms for vertical nutrient transport within a north Atlantic mesoscale eddy, *Deep Sea Res., Part II*, 48(4), 757–773.
- McGillicuddy, D. J. (2016), Mechanisms of physical-biological-biogeochemical interaction at the oceanic mesoscale, *Annu. Rev. Mar. Sci.*, 8, 125–159.
- Nagai, T., A. Tandon, N. Gruber, and J. C. McWilliams (2008), Biological and physical impacts of ageostrophic frontal circulations driven by confluent flow and vertical mixing, *Dyn. Atmos. Oceans*, 45(3), 229–251.
- Nicholson, S.-A., M. Lévy, J. Llorc, S. Swart, and P. M. S. Monteiro (2016), Investigation into the impact of storms on sustaining summer primary productivity in the sub-Antarctic ocean, *Geophys. Res. Lett.*, 43, 9192–9199, doi:10.1002/2016GL069973.
- Niewiadomska, K., H. Claustre, L. Prieur, and F. d'Ortenzio (2008), Submesoscale physical-biogeochemical coupling across the Ligurian current (northwestern Mediterranean) using a bio-optical glider, *Limnol. Oceanogr. Methods*, 53(5part2), 2210–2225.
- Oschlies, A. (2002), Can eddies make ocean deserts bloom?, *Global Biogeochem. Cycles*, 16(4), 1106, doi:10.1029/2001GB001830.
- Pallàs-Sanz, E., J. Candela, J. Sheinbaum, J. Ochoa, and J. Jouanno (2016), Trapping of the near-inertial wave wakes of two consecutive hurricanes in the loop current, *J. Geophys. Res. Oceans*, 121, 7431–7454, doi:10.1002/2015JC011592.
- Pollard, R., and L. Regier (1992), Vorticity and vertical circulation at an ocean front, *J. Phys. Oceanogr.*, 22(6), 609–625.
- Pollard, R. T., and R. C. Millard (1970), Comparison between observed and simulated wind-generated inertial oscillations, *Deep Sea Res. Oceanogr. Abstr.*, 17, 813–821.
- Pollard, R. T., P. B. Rhines, and R. Thompson (1972), The deepening of the wind-mixed layer, *Geophys. Astrophys. Fluid Dyn.*, 4(1), 381–404.
- Powell, J. R., and M. D. Ohman (2015), Covariability of zooplankton gradients with glider-detected density fronts in the southern California current system, *Deep Sea Res., Part II*, 112, 79–90.
- Powell, T. M., C. V. Lewis, E. N. Curchitser, D. B. Haidvogel, A. J. Hermann, and E. L. Dobbins (2006), Results from a three-dimensional, nested biological-physical model of the California current system and comparisons with statistics from satellite imagery, *J. Geophys. Res.*, 111, C07018, doi:10.1029/2004JC002506.
- Price, J. F. (1981), Upper ocean response to a hurricane, *J. Phys. Oceanogr.*, 11(2), 153–175.
- Raven, J., and P. Falkowski (1999), Oceanic sinks for atmospheric CO₂, *Plant Cell Environ.*, 22(6), 741–755.
- Rintoul, S. R., and M. H. England (2002), Ekman transport dominates local air-sea fluxes in driving variability of sub-Antarctic mode water, *J. Phys. Oceanogr.*, 32(5), 1308–1321.
- Rodgers, K. B., O. Aumont, S. Mikaloff Fletcher, Y. Plancherel, L. Bopp, C. de Boyer Montégut, D. Iudicone, R. Keeling, G. Madec, and R. Wanninkhof (2014), Strong sensitivity of southern ocean carbon uptake and nutrient cycling to wind stirring, *Biogeosciences*, 11(15), 4077–4098.
- Rudnick, D., and J. Luyten (1996), Intensive surveys of the Azores front 1. Tracers and dynamics, *J. Geophys. Res.*, 101(C1), 923–939.
- Rumyantseva, A., N. Lucas, T. Rippeth, A. Martin, S. C. Painter, T. J. Boyd, and S. Henson (2015), Ocean nutrient pathways associated with the passage of a storm, *Global Biogeochem. Cycles*, 29(8), 1179–1189.
- Shchepetkin, A. F., and J. C. McWilliams (2005), The regional ocean modeling system (ROMS): A split-explicit, free-surface, topography-following coordinate oceanic model, *Ocean Model.*, 9, 347–404.
- Siedlecki, S., D. Archer, and A. Mahadevan (2011), Nutrient exchange and ventilation of benthic gases across the continental shelf break, *J. Geophys. Res.*, 116, C06023, doi:10.1029/2010JC006365.
- Smolarkiewicz, P. K., and L. G. Margolin (1998), Mpdata: A finite-difference solver for geophysical flows, *J. Comput. Phys.*, 140(2), 459–480.
- Spitz, Y. H., P. A. Newberger, and J. S. Allen (2003), Ecosystem response to upwelling off the Oregon coast: Behavior of three nitrogen-based models, *J. Geophys. Res.*, 108(C3), 3062, doi:10.1029/2001JC001181.
- Steele, J. H., and E. W. Henderson (1992), The role of predation in plankton models, *J. Plankton Res.*, 14(1), 157–172.
- Stephenson, G. R., S. T. Gille, and J. Sprintall (2013), Processes controlling upper-ocean heat content in Drake passage, *J. Geophys. Res. Oceans*, 118, 4409–4423, doi:10.1002/jgrc.20315.
- Stern, M. E. (1965), Interaction of a uniform wind stress with a geostrophic vortex, *Deep Sea Res. Oceanogr. Abstr.*, 12, 355–367.
- Stevenson, J. W., and P. P. Niiler (1983), Upper ocean heat budget during the Hawaii-to-Tahiti shuttle experiment, *J. Phys. Oceanogr.*, 13(10), 1894–1907.
- Strass, V. H., A. C. N. Garabato, R. T. Pollard, H. I. Fischer, I. Hense, J. T. Allen, J. F. Read, H. Leach, and V. Smetacek (2002), Mesoscale frontal dynamics: Shaping the environment of primary production in the Antarctic circumpolar current, *Deep Sea Res., Part II*, 49(18), 3735–3769.
- Taylor, A. G., R. Goericke, M. R. Landry, K. E. Selph, D. A. Wick, and M. J. Roadman (2012), Sharp gradients in phytoplankton community structure across a frontal zone in the California current ecosystem, *J. Plankton Res.*, 34(9), 778–789.
- Taylor, J. R., and R. Ferrari (2010), Buoyancy and wind-driven convection at mixed layer density fronts, *J. Phys. Oceanogr.*, 40(6), 1222–1242.
- Thomas, L., and R. Ferrari (2008), Friction, frontogenesis, and the stratification of the surface mixed layer, *J. Phys. Oceanogr.*, 38(11), 2501–2518.
- Thomas, L. N. (2005), Destruction of potential vorticity by winds, *J. Phys. Oceanogr.*, 35(12), 2457–2466.
- Thomas, L. N., J. R. Taylor, E. A. D'Asaro, C. M. Lee, J. M. Klymak, and A. Shcherbina (2015), Symmetric instability, inertial oscillations, and turbulence at the Gulf Stream front, *J. Phys. Oceanogr.*
- Thompson, A. F., A. Lazar, C. Buckingham, A. C. Naveira Garabato, G. M. Damerell, and K. J. Heywood (2016), Open-ocean submesoscale motions: A full seasonal cycle of mixed layer instabilities from gliders, *J. Phys. Oceanogr.*, 46(4), 1285–1307.
- Volk, T., and M. I. Hoffert (1985), Ocean carbon pumps: Analysis of relative strengths and efficiencies in ocean-driven atmospheric CO₂ changes, in *The Carbon Cycle and Atmospheric CO₂: Natural Variations Archean to Present*, edited by E. T. Sundquist and W. S. Broecker, pp. 99–110, American Geophysical Union, Washington, D. C., doi:10.1029/GM032p0099.
- Weller, R. A. (1982), The relation of near-inertial motions observed in the mixed layer during the JASIN (1978) experiment to the local wind stress and to quasi-geostrophic flow field, *J. Phys. Oceanogr.*, 12, 1122–1136.
- Whitt, D., and L. Thomas (2013), Near-inertial waves in strongly baroclinic currents, *J. Phys. Oceanogr.*, 43, 706–725.
- Whitt, D. B., and L. N. Thomas (2015), Resonant generation and energetics of wind-forced near-inertial motions in a geostrophic flow, *J. Phys. Oceanogr.*, 45, 181–208, doi:10.1175/JPO-D-14-0168.1.
- Zhai, X. (2015), Latitudinal dependence of wind-induced near-inertial energy, *J. Phys. Oceanogr.*, 45(12), 3025–3032.